Fate mapping and scRNA sequencing reveal origin and diversity of lymph node stromal precursors

Elisa Lenti, Luca Genovese, Silvia Bianchessi, Aurora Maurizio, Simona Baghai Sain, Alessia Di Lillo, Greta Mattavelli, Itamar Harel, Francesca Bernassola, Thomas Hehlgans, et al.

Fate mapping and scRNA sequencing reveal origin and diversity of lymph node stromal precursors

Elisa Lenti,[1,14] Luca Genovese,[1,14] Silvia Bianchessi,[1,14] Aurora Maurizio,[2,14] Simona Baghai Sain,[2] Alessia di Lillo,[1] Greta Mattavelli,[1] Itamar Harel,[3] Francesca Bernassola,[4] Thomas Hehlgans,[5] Klaus Pfeffer,[6] Mariacristina Crosti,[7] Sergio Abrignani,[7,8] Sylvia M. Evans,[9] Giovanni Sitia,[10] Nuno Guimarães-Camboa,[11,12] Vincenzo Russo,[1] Serge A. van de Pavert,[13] Jose Manuel Garcia-Manteiga,[2] and Andrea Brendolan[1,15,*]

[1]Division of Experimental Oncology, IRCCS San Raffaele Scientific Institute, Milan, Italy
[2]Center for Omics Sciences, IRCCS San Raffaele Scientific Institute, Milan, Italy
[3]Department of Genetics, The Alexander Silberman Institute of Life Sciences, The Hebrew University of Jerusalem, Edmond J. Safra Campus, Givat Ram, Jerusalem 9190401, Israel
[4]Department of Experimental Medicine, TOR, University of Rome ''Tor Vergata'', Rome 00133, Italy
[5]Leibniz Institute of Immunotherapy (LIT), Chair for Immunology, University of Regensburg, 93053 Regensburg, Germany
[6]Institute of Medical, Microbiology and Hospital Hygiene, University Hospital Düsseldorf, 40225 Düsseldorf, Germany
[7]INGM, Istituto Nazionale di Genetica Molecolare 'Romeo ed Enrica Invernizzi', Milan, Italy
[8]Department of Clinical Science and Community Health (DISCCO), University of Milan, Milan, Italy
[9]Skaggs School of Pharmacy, University of California at San Diego, La Jolla, CA 92093, USA
[10]Division of Immunology, Transplantation and Infectious Diseases, IRCCS San Raffaele Scientific Institute, Milan, Italy
[11]Institute of Cardiovascular Regeneration, Goethe-University, Frankfurt 60590, Germany
[12]German Center for Cardiovascular Research, Berlin (partner site Frankfurt Rhine-Main), Germany
[13]Centre d'Immunologie de Marseille-Luminy (CIML), Aix Marseille Université, INSERM, CNRS, Marseille, France
[14]These authors contributed equally
[15]Lead contact
*Correspondence: brendolan.andrea@hsr.it
https://doi.org/10.1016/j.immuni.2022.03.002

SUMMARY

Lymph node (LN) stromal cells play a crucial role in LN development and in supporting adaptive immune responses. However, their origin, differentiation pathways, and transcriptional programs are still elusive. Here, we used lineage-tracing approaches and single-cell transcriptome analyses to determine origin, transcriptional profile, and composition of LN stromal and endothelial progenitors. Our results showed that all major stromal cell subsets and a large proportion of blood endothelial cells originate from embryonic Hoxb6$^+$ progenitors of the lateral plate mesoderm (LPM), whereas lymphatic endothelial cells arise from Pax3$^+$ progenitors of the paraxial mesoderm (PXM). Single-cell RNA sequencing revealed the existence of different Cd34$^+$ and Cxcl13$^+$ stromal cell subsets and showed that embryonic LNs contain proliferating progenitors possibly representing the amplifying populations for terminally differentiated cells. Taken together, our work identifies the earliest embryonic sources of LN stromal and endothelial cells and demonstrates that stromal diversity begins already during LN development.

INTRODUCTION

Lymph node (LN) stromal cells are organizers of lymphoid compartments and regulators of adaptive immune responses (Brown et al., 2019; Perez-Shibayama et al., 2019; Buckley et al., 2015). In addition to secreting factors for lymphocyte recruitment and survival, stromal cells produce the extracellular matrix (ECM), a network of structural proteins important for lymphocyte locomotion and tissue remodeling. Stromal cells not only secrete factors for lymphocyte recruitment and survival but also produce the ECM, a network of structural proteins important for lymphocyte locomotion and tissue remodeling (Bajénoff et al., 2006; Sixt et al., 2005). Based on phenotypic analysis and tissue distribution, four major, functionally distinct stromal cell subsets have been identified, namely follicular dendritic cells (FDCs) of the B cell follicle, which play an important role in B cell homeostasis; marginal reticular cells (MRCs), which surround the outer region of the follicle and are involved in antigen capture and transport; fibroblastic reticular cells (FRCs) of the T cell zone, which play a critical role in T cell homeostasis and migration; and cells of the perivascular niche, which may function as stromal progenitor cells in the spleen and LNs (Acton et al., 2012; Brown et al., 2019; Camara et al., 2019; Schaeuble et al., 2017; Sitnik et al., 2016; Martinez

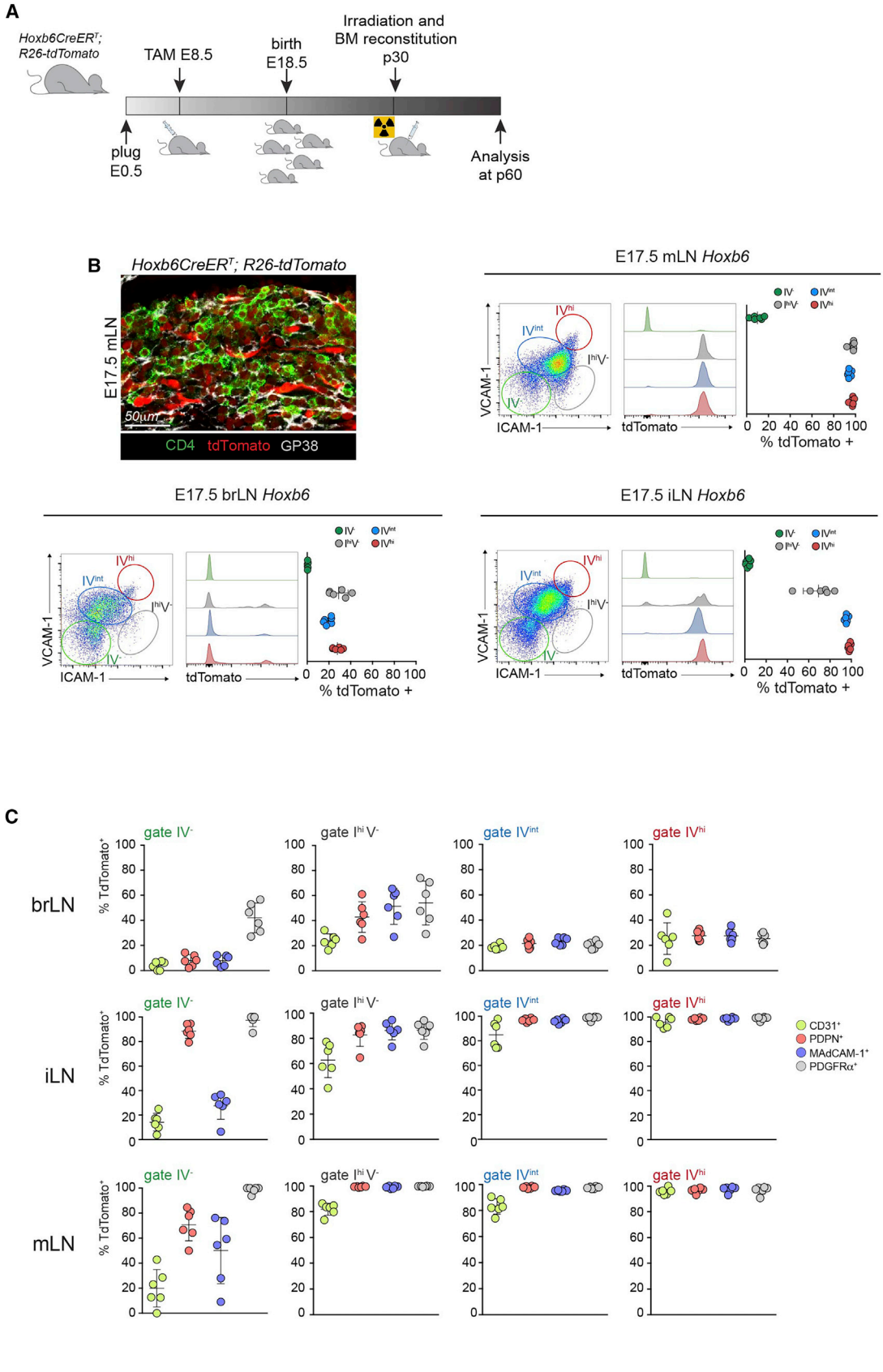
A
Hoxb6CreER^T; R26-tdTomato
TAM E8.5
birth E18.5
Irradiation and BM reconstitution p30
plug E0.5
Analysis at p60
B
Hoxb6CreER^T; R26-tdTomato
E17.5 mLN
50µm
CD4 tdTomato GP38
E17.5 mLN Hoxb6
E17.5 brLN Hoxb6
E17.5 iLN Hoxb6
VCAM-1
ICAM-1
tdTomato
% tdTomato +
C
brLN
iLN
mLN
% TdTomato+
gate IV-
gate IhiV-
gate IVint
gate IVhi
CD31+
PDPN+
MAdCAM-1+
PDGFRα+

et al., 2019; Perez-Shibayama et al., 2019; Thierry et al., 2019). In addition to traditional stromal cells, endothelial cells are also emerging as critical organizers of the lymphoid microenvironment (Bovay et al., 2018; Onder et al., 2013, 2017).

Single-cell RNA sequencing (scRNA-seq) coupled with immunofluorescence has recently revealed the existence of additional stromal cell subsets in adult LN, classified based on gene expression profile and niche-specific distribution (Rodda et al., 2018). Further work provides evidence that the anatomical localization of adult LNs, together with the microenvironment, shapes the transcriptomic and functional profiles of stromal cells (Cording et al., 2014; Pezoldt et al., 2018). Although there is increasing evidence of lymphoid stromal cell diversity, it is not known whether multiple stromal cell subsets are present in embryonic LN and whether their transcriptional differences are acquired during embryonic development or are due to postnatal LN-specific differentiation of stromal progenitors.

Fate-mapping analyses has shown that stromal cells in cervical LN originate neural crest cells (Jarjour et al., 2014). Moreover, embryonic Nestin$^+$ mesenchymal cells can generate the vast majority of mature stromal cells in different LNs (Koning et al., 2016), whereas embryonic Fap$^+$ precursors contribute to different stromal cell subsets in mesenteric LN (Denton et al., 2019). Of note, Nestin$^+$ progenitor cells, unlike Fap$^+$ cells, give rise to blood and lymphatic endothelial cells (BECs and LECs) in the LN. Moreover, it has been shown that stromal cells in the LN of the inguinal region originate from preadipocytes of the fat pad (Bénézech et al., 2012) and that white adipose tissue from inguinal and mesenteric regions originate from Hoxb6$^+$ cells of the lateral plate mesoderm (LPM) at day 8.5 of gestation (Sebo et al., 2018). Nevertheless, whether LPM is the earliest embryonic source of LN stromal cells is still unknown. Endothelial cells in various organs have been reported to originate from both LPM and paraxial mesoderm (PXM) (Prummel et al., 2020; Stone and Stainier, 2019), although the origin of BECs and LEC in LNs remains unclear.

Here, we used lineage-tracing approaches in conjunction with single-cell transcriptome analyses to accurately determine the lineage contribution and the molecular profile of progenitor cells in different LNs along the body axis. Our results show that stromal and BECs arise from LPM Hoxb6$^+$ progenitor cells. In contrast, we found that most lymphatic LECs originate from PXM progenitor cells and that LPM contributes to LECs only in mesenteric LNs. Of note, within the LPM, we identified *Isl1* expressing cells as a lineage that gives rise to stromal and endothelial cells only in the mesenteric and popliteal LNs, indicating the presence of transcriptional differences in stromal progenitor cells of different LNs. scRNA-seq of stromal precursors from different embryonic LNs also revealed the presence of unique subsets of Cd34$^+$ and Cxcl13$^+$ cells, which likely represent the progenitors for more differentiated cells. Our work identifies the earliest embryonic source of LN stromal cells and endothelial cells and demonstrates that stromal diversity begins early during LN development.

RESULTS

The lateral plate mesoderm generates lymphoid tissue organizer cells

LN stromal cells are thought to develop from mesenchymal progenitors (Koning and Mebius, 2020). However, the exact embryonic source of the stromal progenitor cells is still unclear.

To address this question, we performed lineage-tracing experiments by crossing Hoxb6-driven conditional CreERT mice with the R26tdTomato reporter line to achieve specific and temporally controlled recombination in LPM after tamoxifen administration

(Nguyen et al., 2009; Srinivas et al., 2001). Pregnant mice were injected with a single dose of tamoxifen at E8.5 to induce sustained expression of tdTomato, and the contribution of early LPM precursors to embryonic LN was assessed at gestation E14.5 and E17.5 by immunofluorescence and flow cytometry analyses (Figures 1A, 1B, and S1A). The results showed that GP38$^+$tdTomato$^+$ cells were already present in the presumptive anlage of the mesenteric LN along with small clusters of CD4$^+$ lymphoid tissue inducer (LTi) cells at both time points examined (Figures 1B and S1A).

We then performed flow cytometry analysis to quantify the contribution of LPM progenitor cells to the brachial, inguinal, and mesenteric E17.5 LN representative of three different anatomical locations along the body axis. Previous work has shown that expressions of ICAM-1 (I) and VCAM-1 (V) identify distinct subsets of lymphoid tissue organizers (LTo), including endothelial cells (Bénézech et al., 2010). Analysis of tdTomato$^+$ cells showed that almost all LPM progenitors contributed to the IV^{int} and I^{hi}V$^-$ and IV^{hi} LTo cell populations expressing stromal (MAdCAM-1, GP38, and PDGFRα) and endothelial (CD31) markers in the inguinal and mesenteric LNs, although the contribution to the brachial LNs was about 30% (Figures 1B, 1C, and S1B). Of note, LPM did not contribute to the IV$^-$ subset in any of the LN examined (Figure 1B). These results suggest that the E8.5 progenitors of the LPM differentiate to give rise to distinct subsets of stromal and endothelial progenitors of the developing LNs.

Figure 1. Lateral plate mesoderm-derived Hoxb6 progenitors contribute to embryonic LTo

(A) Schematic representation of the lineage-tracing strategy in *Hoxb6CreER^T;R26-tdTomato* mice.

(B) Representative confocal images of *Hoxb6CreER^T;R26-tdTomato* embryonic E17.5 mLN sections stained for RFP, as marker of Hoxb6 lineage-traced cells (red), CD4 (green), and GP38/PDPN (gray), as markers for LTi and LTo cells, respectively. Scale bars represent 50 μm. Data are representative of 4–5 embryos analyzed.

Representative FACS analysis of tdTomato expression by ICAM-1/VCAM-1 embryonic LN cells IV$^-$ (green), I^{hi}V$^-$ (gray), IV^{int} (blue), IV^{hi} (red) in brLN, mLN, and iLNs isolated from E17.5 *Hoxb6CreER^T;R26-tdTomato* embryos.

(C) Representative FACS analysis of the percentages of IV$^-$, I^{hi}V$^-$, IV^{int}, and IV^{hi} cells expressing GP38/PDPN, MAdCAM-1, PDGFRα, and CD31 in brLN, iLN, and mLN from E17.5 *Hoxb6CreER^T;R26-tdTomato* embryos.

Results are representative of 6 independent experiments, each performed with 4–6 pooled embryos. brLN, brachial LN; iLN, inguinal LN; mLN, mesenteric LN. See also Figures S1 and S2.

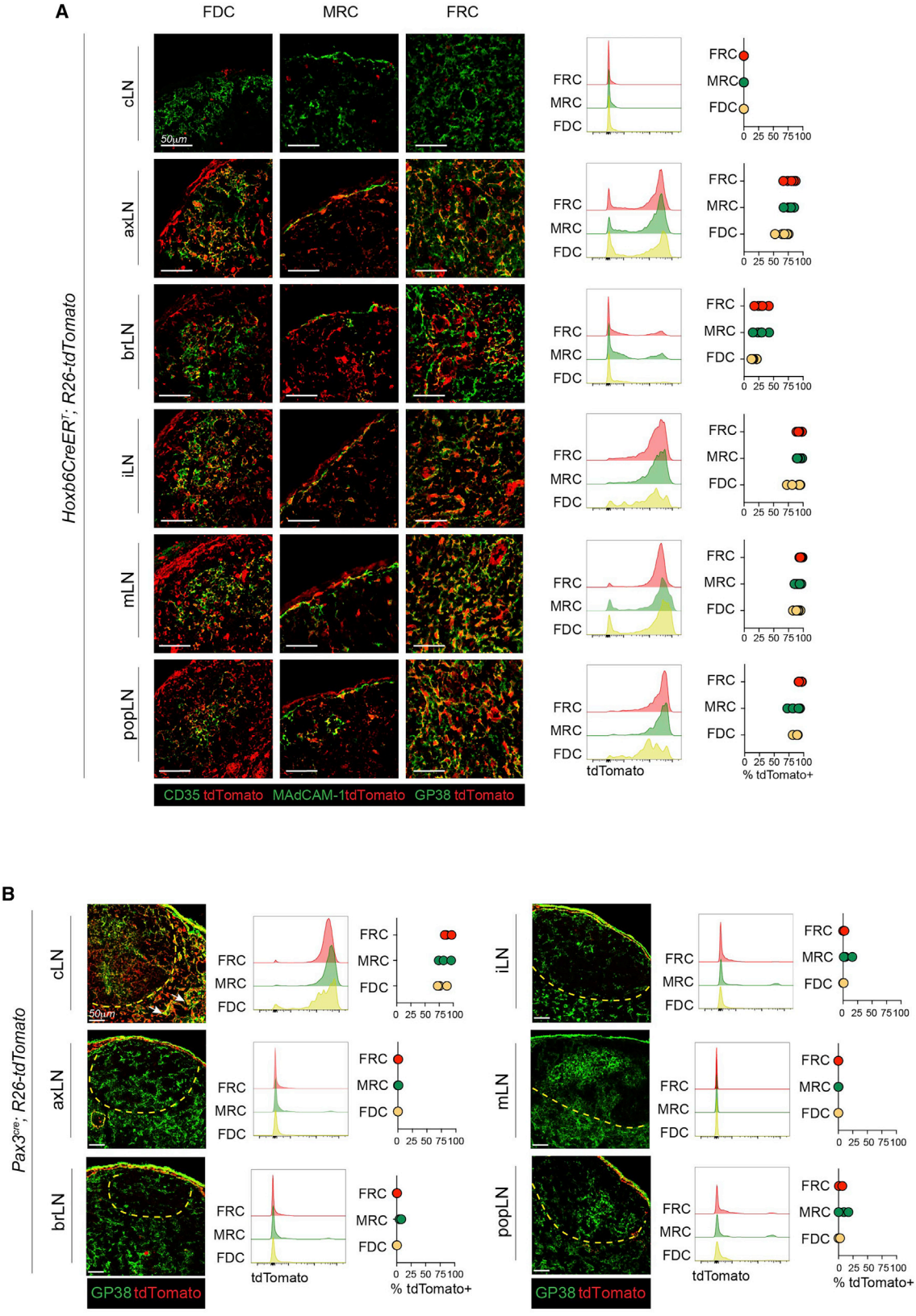
A
FDC
MRC
FRC
Hoxb6CreER^{T}; R26-tdTomato
cLN
axLN
brLN
iLN
mLN
popLN
50μm
CD35 tdTomato
MAdCAM-1tdTomato
GP38 tdTomato
FRC
MRC
FDC
0 25 50 75100
tdTomato
% tdTomato+
B
Pax3^{cre}; R26-tdTomato
cLN
axLN
brLN
iLN
mLN
popLN
50μm
GP38 tdTomato
FRC
MRC
FDC
tdTomato
0 25 50 75100
% tdTomato+

Progenitors of the lateral plate mesoderm generate all mature lymph node stromal cells

To determine the relationship between tdTomato$^+$ LTo cells and mature stromal cell subsets, we analyzed adult cervical, brachial, axillary, inguinal, mesenteric, and popliteal LN from *Hoxb6^{CreERT};R26tdTomato* compound mice injected with a single dose of tamoxifen at E8.5 to mark LPM. Since it is known that Hoxb6$^+$ LPM progenitor cells also give rise to the hematopoietic compartment, mice were lethally irradiated 2 months after tamoxifen injection and reconstituted with wild-type bone marrow cells to remove tdTomato-labeled hematopoietic cells that could confound the analysis. Our results showed that in all LNs, except cervical LNs, tdTomato-derived cells contributed to the three major stromal cell subsets, namely: GP38$^+$ FRCs, CD35$^+$ FDCs, and MAdCAM-1$^+$ MRCs (Figures 2A and S1C). Flow cytometry analysis of cells isolated from single adult LNs confirmed that >85% of axillary, inguinal, mesenteric, and popliteal and 25% of brachial GP38$^+$ FRCs, CD35$^+$ FDCs, MAdCAM-1$^+$ MRCs, and DN cells were LPM derived, whereas no contribution was observed in cervical LNs reportedly derived from neural crest cells (Figures 2A, S1C, and S1D).

The PXM is known to give rise to cells in various organs such as bone, dermis, skeletal muscle, and endothelium during embryonic development (Buckingham and Rigby, 2014; Stone and Stainier, 2019; Tani et al., 2020). To assess the potential contribution of this mesodermal layer to adult stromal cells, we crossed constitutive *Pax3$^{Cre/+}$* mice, in which Cre expression is driven by the PXM transcription factor Pax3, with the *R26dTomato* reporter (Madisen et al., 2010).

Immunofluorescence analyses in conjunction with flow cytometry performed on adult *Pax3$^{Cre/+}$;R26dTomato* compound mice revealed that with the exception of cervical LNs, where *Pax3* is known to be expressed in neural crest cells (Betancur et al., 2010), the PXM did not contribute to the stromal cells of all other LNs analyzed (Figures 2B and S1D). Overall, these results clearly show that the LPM is the only mesodermal layer that gives rise to LN stromal cells.

Lymph node-specific lineages contribute to the stromal cell pool

We have previously shown that a subset of LPM progenitors expressing Hoxb6 and Nkx2.5 can generate spleen but not LN stroma (Castagnaro et al., 2013; Lenti et al., 2016). These results suggest that LPM contains distinct lineages that express unique transcription factors and can generate phenotypically and functionally similar mature stromal cells (e.g., FDCs) in different LNs. To test this hypothesis, we performed lineage tracing by crossing R26tdTomato reporter mice with a knockin allele that constitutively expresses Cre recombinase under the control of Isl1, a gene encoding a transcription factor expressed in LPM progenitors that contributes to splenic stromal progenitors (Castagnaro et al., 2013; Yang et al., 2006). We analyzed the contribution of Isl1 progeny to the developing mesenteric LN and found tdTomato$^+$ cells in the developing mesenteric LN at E14.5 and E17.5 along with CD4$^+$ LTi cells (Figure 3A). Notably, although *Isl1* mRNA was detected at E17.5 and postnatal day 2 (P2) only in mesenteric LNs, ISL1 protein was present at E17.5 only in a few cells near the developing LN anlage and was absent postnatally (Figures S2A and S2B). These results indicate that *Isl1* expression occurs earlier in development, and this notion is supported by previous findings showing expression of *Isl1* at E8.5 in the LPM, splanchnic mesoderm of the gut, and in the developing limb buds, all derivatives of the LPM (Zhuang et al., 2013).

Flow cytometry analysis at E17.5 also revealed a unique pattern of Isl1 contribution to various lymphoid LTo cell subsets, accounting for nearly 80%–100% of IV^{int} and I^{hi}V$^-$ and IV^{hi} LTo cells of the mesenteric LN, whereas the contribution to the inguinal and brachial LN was 20% and absent, respectively, for these populations (Figures 3A and S2C). Of note, the contribution to the IV$^-$ subgroup was negligible in all LNs analyzed. These and previous results support the idea that at E8.5 of embryonic development, different transcription factors mark LPM precursors that differentiate into stromal and endothelial precursors of the developing LNs.

We then examined the contribution of this lineage to adult stromal cells by analyzing adult compound mice that were lethally irradiated and reconstituted with wild-type bone marrow to exclude recombination in the hematopoietic lineage. 2 months after hematopoietic reconstitution, immunofluorescence analysis combined with flow cytometry on cells isolated from mesenteric and popliteal LN showed that >85% of GP38$^+$ FRCs, CD35$^+$ FDCs, MAdCAM-1$^+$ MRCs, and DN cells were tdTomato$^+$ and thus derived from Isl1$^+$ progeny (Figure 3B). In contrast, the stromal cells of the cervical, axillary, brachial, and inguinal LN were not tdTomato$^+$ (Figure 3B), supporting the hypothesis that although the stromal cells of LN are derived from progenitor cells of LPM, the stroma of each LN is derived from different subsets of the LPM lineages, as characterized by the expression of different transcription factors. Finally, we investigated whether the Isl1$^+$ lineage plays a functional role in LN organogenesis by knocking down LTβR signaling. We generated *Ltβr$^{flox/flox}$;Isl1-$^{Cre/+}$* and control mice and analyzed the gross morphology of various adult LNs and spleen after 6 weeks. Interestingly, loss

Figure 2. Lymph node stromal cell subsets originate from the lateral plate mesoderm

(A) Representative confocal images of *Hoxb6CreER^T;R26-tdTomato* adult LN sections stained for RFP (red), as marker of Hoxb6 lineage-traced cells, CD35, MAdCAM-1 and GP38/PDPN (green) as markers for FDCs, MRCs, and FRCs, respectively. Scale bars represent 50 μm. Data are representative of 10 mice analyzed for each panel. On the right, representative histograms of tdTomato mean fluorescent intensity and percentage of tdTomato$^+$ cells in LN stromal cells isolated from *Hoxb6CreER^T; R26-tdTomato* adult mice. Data are representative of 5 independent experiments, each performed with pooled LNs from 2 mice.
(B) Representative confocal images of *Pax3$^{Cre/+}$;R26-tdTomato* adult LN sections stained for tdTomato (red), as marker of Pax3 lineage-traced cells, and GP38 (green), as markers for FRC. Scale bars represent 50 μm. Data are representative of 5 mice analyzed for each panel. Representative histograms of tdTomato mean fluorescent intensity and percentage of tdTomato$^+$ cells in LN stromal cells isolated from *Pax3$^{Cre/+}$;R26-tdTomato* mice. Data are representative of 3 independent experiments, each performed with pooled LNs from 2 mice.
cLN, cervical LN; axLN, axillary LN; brLN, brachial LN; iLN, inguinal LN; mLN, mesenteric LN; popLN, popliteal LN.
See also Figure S1.

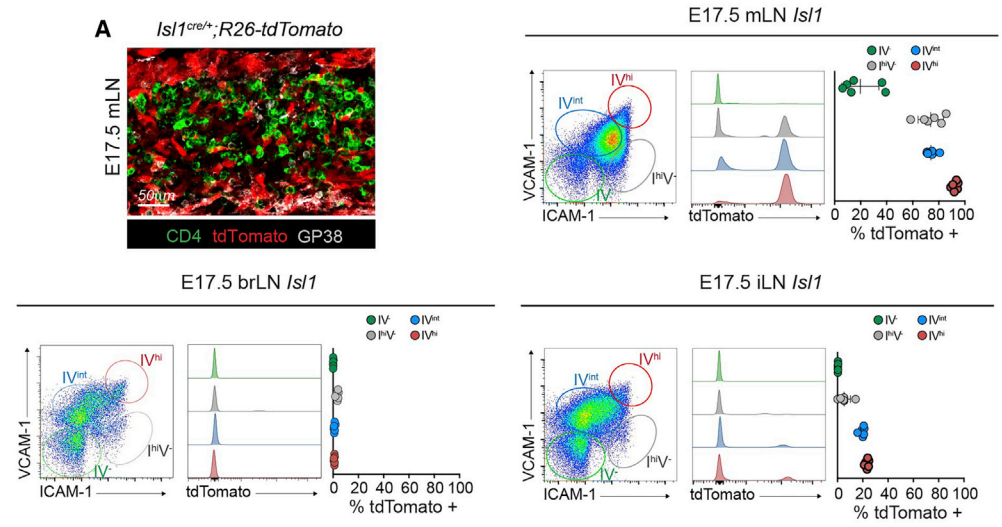
A
Isl1cre/+;R26-tdTomato
E17.5 mLN
50μm
CD4 tdTomato GP38
E17.5 mLN Isl1
E17.5 brLN Isl1
E17.5 iLN Isl1
IV-
IVint
IVhi
IhiV-
VCAM-1
ICAM-1
tdTomato
0 20 40 60 80 100
% tdTomato +

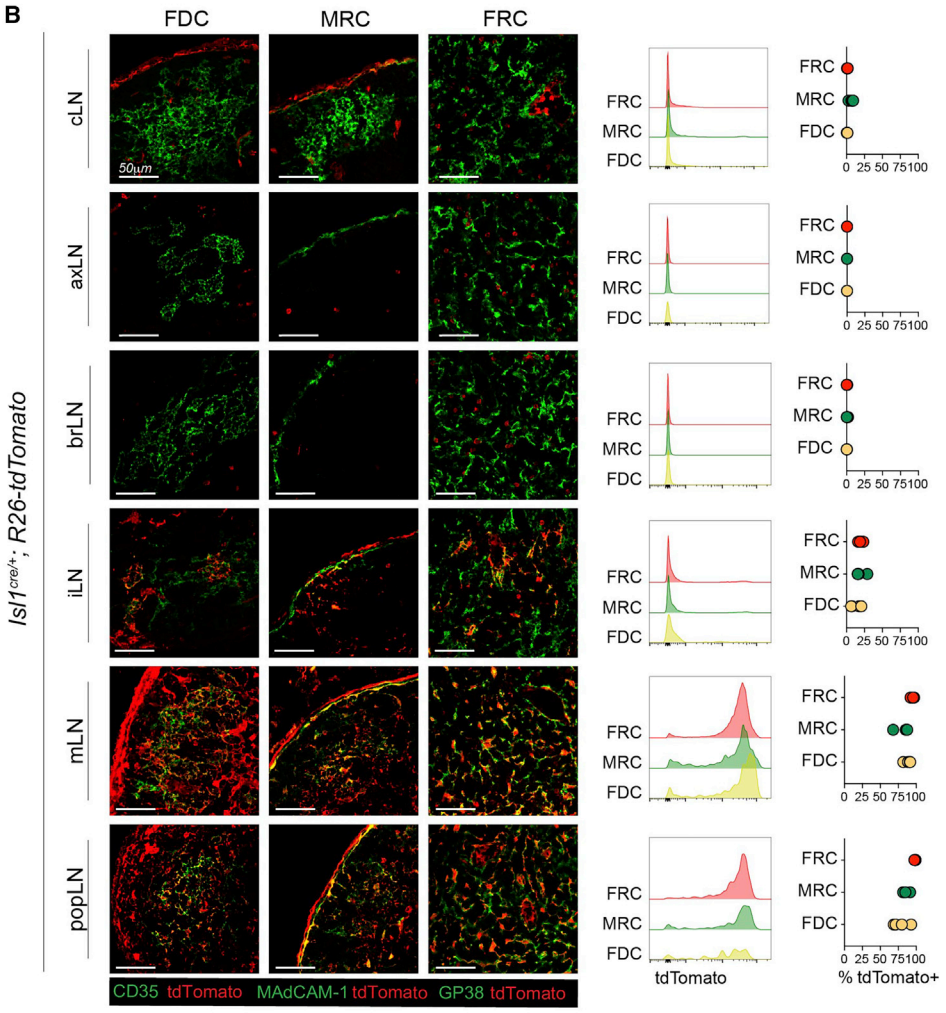
B
FDC
MRC
FRC
cLN
axLN
brLN
iLN
mLN
popLN
Isl1cre/+; R26-tdTomato
50μm
FRC
MRC
FDC
0 25 50 75100
CD35 tdTomato MAdCAM-1 tdTomato GP38 tdTomato
tdTomato
% tdTomato+

of LTβR signaling in the Isl1$^+$ lineage prevented the development of the popliteal LN and caused severe hypoplasia of the mesenteric LN, whereas the inguinal LNs were not affected (Figure S3A).

Immunofluorescence analysis of the mesenteric and inguinal LNs revealed normal organization of B220$^+$ and CD3$^+$ cell clusters and the presence of intact CD35$^+$ FDC networks. Consistent with the contribution of Isl1 to splenic stromal cells and the requirement of LTβR signaling for splenic organization, the formation of T and B cell clusters and FDC networks in the spleen was severely impaired in *Ltβr$^{flox/flox}$;Isl1$^{Cre/+}$* compared with controls (Figure S3B). Taken together, these results demonstrate the importance of the Isl1 lineage specifically in supporting organogenesis of the popliteal and mesenteric LNs and suggest that the organization of T and B cell clusters in the mesenteric LNs is not dependent on LTβR signaling from Isl1-derived stromal cells.

Distinct mesodermal origin of lymph node blood and lymphatic endothelial cells

It is well known that the mesoderm gives rise to BECs and LECs of the developing embryo (Prummel et al., 2020), and recent evidence has shown that the LECs outside the LN originate from the Pax3$^+$ PXM (Stone and Stainier, 2019). However, the exact mesodermal lineages that generate BECs and LECs in LNs are currently unknown. To address this question, we performed lineage-tracing experiments using *Hoxb6CreER^T, Pax3$^{Cre/+}$*, and *Isl1$^{Cre/+}$* mice crossed with the reporter line *R26dTomato* to trace the progeny of the LPM and PXM, respectively (Engleka et al., 2005).

Immunofluorescence in conjunction with flow cytometric analysis showed that the *Hoxb6*$^+$ LPM generates various CD31$^+$Lyve1$^-$ (>85%) BECs, including CD31$^+$PNAd$^+$ cells of the high endothelial venules (HEVs) of the mesenteric and popliteal LNs, whereas the contribution to the endothelium of the brachial, axillary, and inguinal LNs ranged between 40% and 50%, and no contribution to the cervical LN vasculature was observed (Figures 4A and 4B). Notably, the Isl1 lineage contributed to 50%–60% of BECs and HEVs, whereas the contribution to these cells in the brachial, axillary, and inguinal LNs was negligible. Conversely, analysis of the Pax3$^+$ lineage revealed no contribution of PXM to BECs (Figures 4A and 4B). Instead, PXM contributed to >90% of subcapsular and medullary LYVE-1$^+$ CD31$^+$ LECs in the inguinal, axillary, brachial, and popliteal LNs, whereas LECs in the mesenteric LNs were derived from the Hoxb6$^+$ LPM (Figures 4A and 4B). Of note, the PNAD$^+$ HEVs in the brachial and inguinal LNs contained some cells derived from the Pax3$^+$ lineage (Figure 4B), although such a contribution was not observed for all other LN analyzed. Overall, these results show that in the LN, LPM progenitor cells contribute to both BECs and mesenteric LECs, whereas the PXM but not the LPM generated LECs in all superficial LNs analyzed (Figure 4C).

Single-cell transcriptomic analysis of stromal progenitors reveals differences in gene expression across LNs

The differential contribution of Isl1 lineage to stromal and endothelial cells of the brachial, inguinal, and mesenteric LN suggests the existence of distinct embryonic lineages within the LPM that contribute to adult stromal and endothelial cells. Such lineage diversity implies the presence of LN-specific transcription factors as the result of differential positional identity of LNs along the body axis. To address this question, we performed scRNA-seq on cells isolated from the LN of embryonic and neonatal wild-type mice. This strategy was preferred because our lineage-specific reporters showed differential contribution to stromal and endothelial cells, which may have resulted in a mixed population of cells, some expressing tdTomato and others not. We isolated embryonic (E17.5) IV^{hi} LTo cells because they are considered precursors to adult stromal cells, which we found to arise from the Hoxb6$^+$ LPM, as well as cells from postnatal day 2 LNs (Figure S1B). These time points were chosen because the cells are still largely undifferentiated and unaffected by external stimuli, such as mature lymphocytes and the microbiota.

Initially, data were pooled without an integrative alignment procedure to exclude possible batch effects. Samples showed an overlap of common clusters, and we focused our analysis on those expressing known nonhematopoietic and nonendothelial cell markers (Figure S4A).

We then analyzed at low resolution embryonic and neonatal datasets separately after integrating the three LN districts together. We identified three groups of cells, namely Cd34$^+$ SC, Cxcl13$^+$ SC, and Acta2$^+$ mural cells (MuCs), a perivascular group of cells that includes pericytes and smooth muscle cells (Figures 5A and 5B). The Cd34$^+$ SC cluster was predominant at E17.5, whereas the Cxcl13$^+$ SC and MuC clusters were more represented at P2 (Figure 5C).

Top 25 differentially expressed genes (DEGs) at embryonic and neonatal stages showed expression of common markers such as *Col3a1*, *Ly6a/Sca-1*, *Cdknc*, and *Mfap5* for Cd34$^+$ SC; *Ccl19*, *Madcam-1*, and *Tnfsf11* for Cxcl13$^+$ SC; and *Acta2*, *Myl9*, and *Crip1* for MuC (Figures 5D and 5E; Tables S1 and S2).

Figure 3. Mesodermal progenitors of the Isl1 lineage contribute to embryonic LTo

(A) Representative confocal images of *Isl1$^{Cre/+}$;R26-tdTomato* embryonic E17.5 mLN sections stained for RFP (red), as marker of Islet1 lineage-traced cells, CD4 (green) and GP38/PDPN (gray), as markers for LTi and LTo cells, respectively. Scale bars represent 50 μm. Data are representative of 4–5 embryos analyzed for each panel.

Representative FACS analysis of tdTomato expression by ICAM-1/VCAM-1 embryonic LN cells IV$^-$ (green), I^{hi}V$^-$ (gray), IV^{int} (blue), and IV^{hi} (red) in brLN, mLN, and iLNs isolated from E17.5 *Isl1$^{Cre/+}$;R26-tdTomato* embryos. Results are representative of 6 independent experiments, each performed with 4–6 pooled embryonic LNs.

(B) Representative confocal images of *Isl1$^{Cre/+}$;R26-tdTomato* adult LN sections stained for RFP (red), as marker of Isl1 lineage-traced cell, CD35, MAdCAM-1 and GP38/PDPN (green) as markers for FDCs, MRCs, and FRCs, respectively. Scale bars represent 50 μm. Data are representative of 12 mice analyzed.

On the right, representative histograms of tdTomato mean fluorescent intensity and percentage of tdTomato$^+$ cells in LN stromal cells isolated from *Isl1$^{Cre/+}$;R26-tdTomato* mice. Data are representative of 4 independent experiments, each performed with pooled LNs from 2 mice.

cLN, cervical LN; axLN, axillary LN; brLN, brachial LN; iLN, inguinal LN; mLN, mesenteric LN; popLN, popliteal LN.

See also Figures S1 and S2.

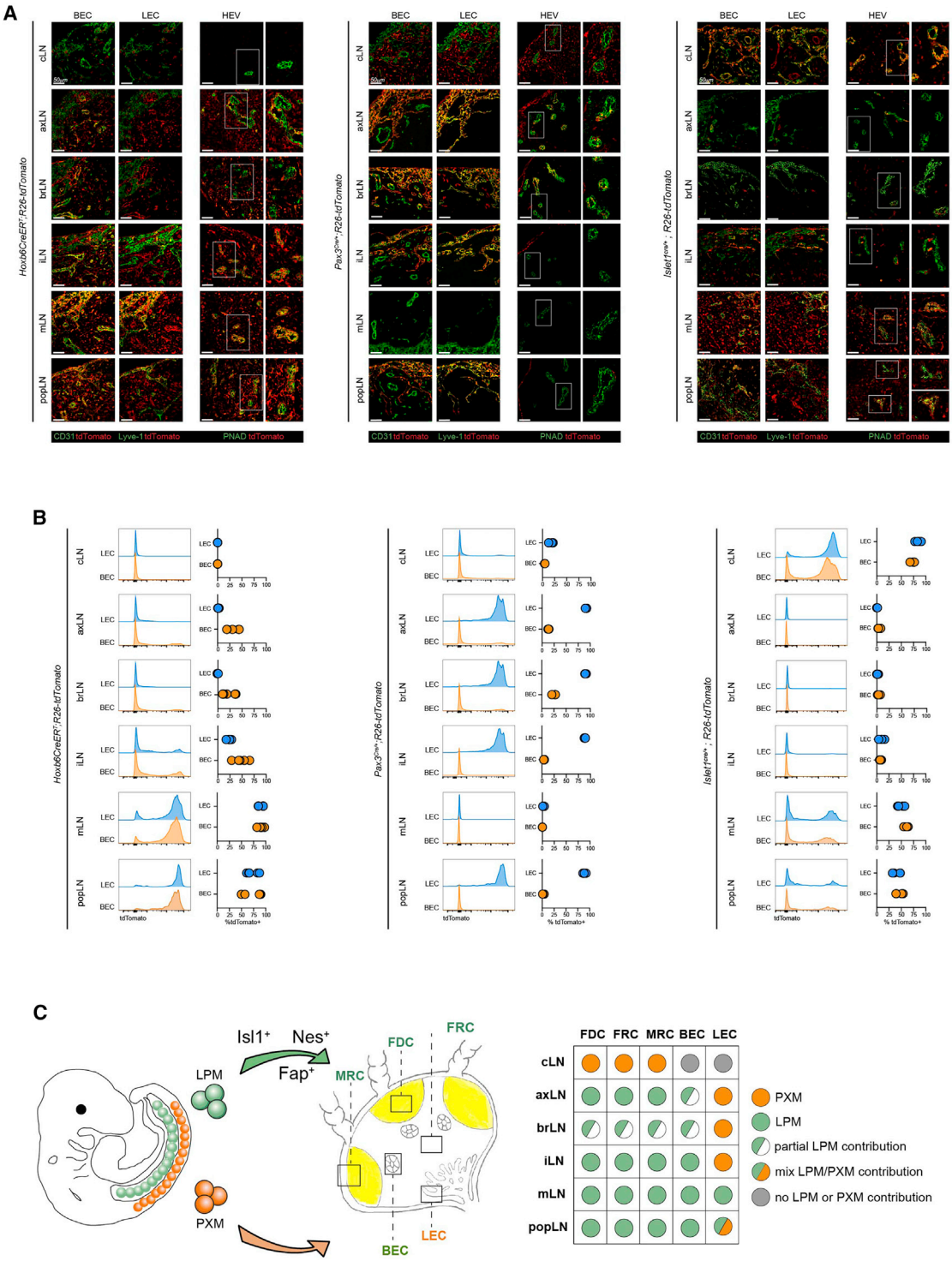

Figure 4. The paraxial mesoderm is the source of lymphatic endothelial cells in LNs

(A) Representative confocal images of *Hoxb6CreER^{T};R26tdTomato*, *Pax3$^{Cre/+}$;R26-tdTomato* and *Isl1$^{Cre/+}$;R26-tdTomato* adult LN sections stained for tdTomato (red), as marker of lineage-traced cells, and CD31, PNAD, or LYVE-1 (green) as markers for BEC, HEV, and LEC, respectively. Scale bars represent 50 μm. Data are representative of 6–10 mice analyzed for each genotype.

(B) Representative histograms of tdTomato mean fluorescent intensity and percentage of tdTomato^{+} cells in LN blood (BEC) and lymphatic (LEC) endothelial cells isolated from *Hoxb6CreER^{T};R26-tdTomato*, *Pax3$^{Cre/+}$;R26-tdTomato* and *Isl1$^{Cre/+}$;R26-tdTomato* mice. Data are representative of 3–5 experiments, each performed with pooled LNs from 2 mice.

DEGs analysis across LN districts and developmental time points revealed transcriptional differences particularly between mesenteric versus superficial (brachial and inguinal) LNs (Figure S4B; Tables S3 and S4). Indeed, the Cd34$^+$ SC cluster showed a higher number of genes differentially expressed (| log2 fold change| > 1) between superficial (inguinal and brachial) versus mesenteric LNs at the embryonic, compared with postnatal stage (Figure S4C; Table S5). Instead, the Cxcl13$^+$ SC cluster showed minor differences in embryonic LNs compared with postnatal LNs (Figure S4C; Table S5). Notably, differences in gene expression in the MuC cluster between superficial and mesenteric LNs were more pronounced postnatally compared with embryonic stage, possibly reflecting a higher number of differentiating cells at this developmental time point (Figure S4C; Table S5). These findings indicate that variations in gene expression among stromal cells are mostly found between superficial versus mesenteric LNs.

Embryonic LNs contain multiple subsets of Cd34$^+$ and Cxcl13$^+$ cells

Previous work has identified distinct SC clusters in adult LN (Rodda et al., 2018; Pezoldt et al., 2018), although it is not known whether these arise from pre-existing distinct embryonic clusters or result from postnatal diversification of a homogeneous cellular population. As our results indicated the existence of three major subsets of cells (Cd34$^+$, Cxcl13$^+$, and MuC), we decided to further investigate their heterogeneity by reanalyzing embryonic and postnatal nonhematopoietic and nonendothelial stromal cells at higher resolution (Figure 6).

Based on differential gene expression, we identified ten embryonic and eleven postnatal clusters distributed on the uniform manifold approximation and projection (UMAP) plot (Figures 6A–6D). At embryonic stages, we identified three clusters of Cxcl13$^+$ cells, six Cd34$^+$ populations, and one cluster of MuC, whereas at neonatal stages, we found four clusters of Cxcl13$^+$ cells, four Cd34$^+$ populations, and three clusters of MuC (Figures 6A–6D; Tables S6 and S7). Of note, UMAP visually revealed a redistribution of Cxcl13$^+$ and Cd34$^+$ clusters during the transition from embryonic to postnatal stages, highlighting the underlying differentiation process and transcriptional changes of the different clusters (Figures 6A and 6B). Analysis of the most differentially expressed markers showed that the gene expression profile of each cluster varied depending on the position of the LN (Figures 6E and 6F), further confirming that the location of the LN along the body axis influences the transcriptomic profile of stromal cell clusters.

At embryonic stages, we found three Cd34$^+$ clusters (0, 1, and 2) showing higher expression of proliferating markers of G_2M phase (e.g., *Top2a*, *Cenpf*, and *Hmgb2*), S phase (e.g., *Ccne2*, *Pclaf* and *Pcna*), and G1/G_2M (e.g., *Ccnb2*, *Cenpa*, and *Hmgb1*). In addition, cluster 3 expressed markers such as *Lpl*, *Aspn*, and *Gsn* associated with TGFβ regulation of ECM; cluster 4 expressed markers of mesothelial origin such as *Krt19*, *Msln*, *Upk3b*, and *Lgals7*; and cluster 5 expressed markers associated with more mature cells including *Igfbp6*, *Ly6a*, and *Pi16* (Figures 6A, 6E, and S5A; Table S6). Notably, cluster 4 was found only in mesenteric LNs. Moreover, the analysis revealed Cxcl13$^+$ cluster 1, showing markers of cellular proliferation such as *Top2a, Prc1*, and two additional Cxcl13$^+$ clusters (8 and 9) expressing markers associated with FRCs including *Ccl19*, *Ccl21*, *Bst2*, *Tnfsf11*, and *Desmin* (Figures 6A, 6C, and 6E).

Similarly, at neonatal stages, we identified four Cd34$^+$ clusters (0, 1, 2, and 3) expressing markers associated with TGFβ regulation of ECM receptor interactions such as *Col1a1*, *Col4a1*, *Lpl*, *Mgp*, and *S100a6* (Figures 6B, 6D, 6F, and S5B). Analysis further revealed three clusters (4, 5, and 6), reflecting subsets of MuC expressing *Rgs5*, *Kcnj8*, and *Col4a1* pericyte markers (cluster 4); *Acta2*, *Myl11*, and *Mef2c* (cluster 5); and *Actg2*, *Cnn1*, and *Myl9* (cluster 6) smooth muscle cell markers (Muhl et al., 2020; Vanlandewijck et al., 2018). In addition, we identified two proliferating Cxcl13$^+$ clusters expressing markers associated with DNA replication such as *Top2a*, *Tclaf*, and *Birc5* (cluster 7) and mitotic G2/M phase such as *Cenpa*, *Cenpf*, and *Cdc20* (cluster 8), possibly reflecting a homogeneous cluster at different stages of the cell cycle. The analysis also revealed two more differentiated clusters (9 and 10) expressing markers of FRCs such as *Ccl19*, *Clu*, *Mfge8*, *Cxcl12*, and *Desmin* (Figures 6B, 6D, 6F, and S5B). Together, these findings demonstrated that embryonic LNs already contain multiple clusters of Cd34$^+$, Cxcl13$^+$, and MuC cells and indicated that stromal diversity is acquired very early during LN development.

We then assessed the spatial localization of the different subpopulations by performing immunofluorescence analysis using antibodies to cluster-specific markers on embryonic and neonatal LNs. We identified the LN primordium by staining hematopoietic cells and the developing ECM with CD45 and collagen 4a1 antibodies, respectively (Figure S5C). Next, we analyzed the distribution of the putative clusters and found the presence of CD34$^+$ nonendothelial cells distributed in the capsule, surrounding vessels, and within the developing LNs (Figure S5C). We also detected LY6A$^+$ and αSMA$^+$ cells corresponding to distinct Cd34$^+$ subclusters (Figures 6 and S5C). Furthermore, we also detected MAdCAM-1, CXCL13, DESMIN, and CCL21, indicative of FRC clusters belonging to the Cxcl13$^+$ clusters (Figure S5C). These results revealed the distribution of distinct nonendothelial cell populations in embryonic and neonatal LNs and reinforced the idea that acquisition of stromal diversity in the CD34$^+$ and Cxcl13$^+$ populations occurs early during LN development.

Stromal cell clusters across developmental stages maintain transcriptional similarities

The presence of different stromal cell subsets at early stages of organogenesis raised the question of whether embryonic, neonatal, and adult stromal cells share transcriptional similarities.

To address this, we sorted CD45$^-$GP38$^+$ LN cells from brachial, inguinal, and mesenteric LN of adult mice and

(C) Proposed model for the origin of stromal and endothelial progenitors. During embryonic development, the Hoxb6$^+$ LPM generates all major stromal cell subsets. The LPM contains different lineages of mesoderm progenitors contributing to specific LNs. The LPM also generates a large proportion of BECs in most LNs, with the PXM making only a modest contribution to brachial BECs. On the contrary, the Pax3$^+$ PXM generates LECs in most LN analysed.
cLN, cervical LN; axLN, axillary LN; brLN, brachial LN; iLN, inguinal LN; mLN, mesenteric LN; popLN, popliteal LN.

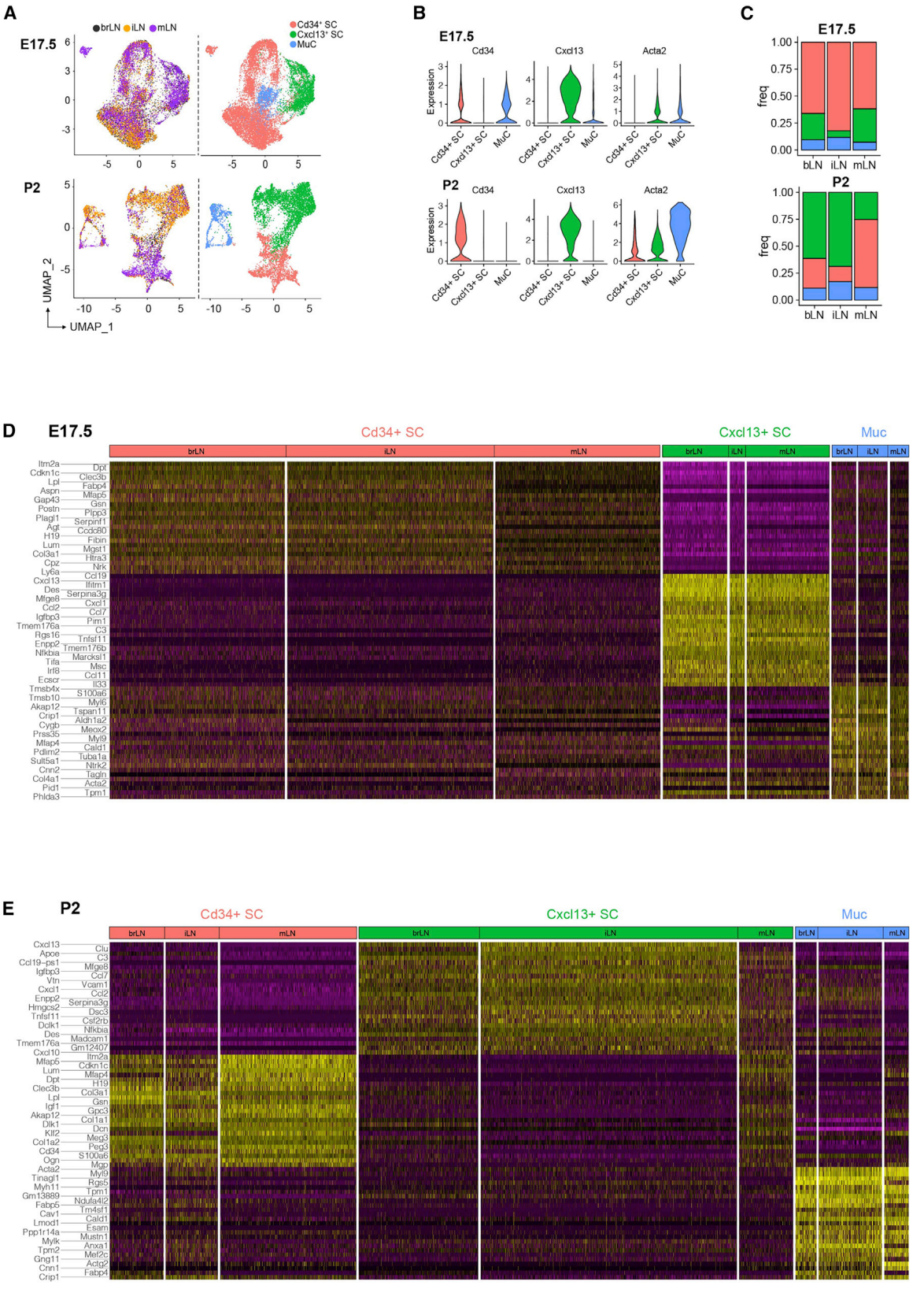
A
E17.5
P2
brLN iLN mLN
Cd34+ SC
Cxcl13+ SC
MuC
UMAP_1
UMAP_2
B
E17.5
P2
Cd34
Cxcl13
Acta2
Expression
C
E17.5
P2
freq
bLN iLN mLN
D
E17.5
Cd34+ SC
Cxcl13+ SC
Muc
brLN iLN mLN
Itm2a Cdkn1c Lpl Aspn Gap43 Postn Plagl1 Agt H19 Lum Col3a1 Cpz Ly6a Cxcl13 Des Mfge8 Ccl2 Igfbp3 Tmem176a Rgs16 Enpp2 Nfkbia Tifa Irf8 Ecscr Tmsb4x Tmsb10 Akap12 Crip1 Cygb Prss35 Mfap4 Pdlim2 Sult5a1 Cnn2 Col4a1 Pid1 Phlda3
Dpt Clec3b Fabp4 Mfap5 Gsn Plpp3 Serpinf1 Ccdc80 Fibin Mgst1 Htra3 Nrk Ccl19 Ifitm1 Serpina3g Cxcl1 Ccl7 Pim1 C3 Tnfsf11 Tmem176b Marcksl1 Msc Ccl11 Il33 S100a6 Myl6 Tspan11 Aldh1a2 Meox2 Myl9 Cald1 Tuba1a Ntrk2 Tagln Acta2 Tpm1
E
P2
Cd34+ SC
Cxcl13+ SC
Muc
brLN iLN mLN
Cxcl13 Apoe Ccl19-ps1 Igfbp3 Vtn Cxcl1 Enpp2 Hmgcs2 Tnfsf11 Dclk1 Des Tmem176a Cxcl10 Mfap5 Lum Dpt Clec3b Lpl Igf1 Akap12 Dlk1 Klf2 Col1a2 Cd34 Ogn Acta2 Tinagl1 Myh11 Gm13889 Fabp5 Cav1 Lmod1 Ppp1r14a Mylk Tpm2 Gng11 Cnn1 Crip1
Clu C5 Mfge8 Ccl7 Vcam1 Ccl2 Serpina3g Dsc3 Csf2rb Nfkbia Madcam1 Gm12407 Itm2a Cdkn1c Mfap4 H19 Col3a1 Gsn Gpc3 Col1a1 Dcn Meg3 Peg3 S100a6 Mgp Myl9 Rgs5 Tpm1 Ndufa4l2 Tm4sf1 Cald1 Esam Mustn1 Anxa1 Mef2c Actg2 Fabp4

performed scRNA-seq to identify mature stromal cell subsets (Figure S6; Table S8). This analysis revealed a distribution of 12 clusters in the UMAP that were equally represented in all LN districts. These clusters were characterized by the expression of unique markers and corresponded to cell populations previously described (Rodda et al., 2018; Pezoldt et al., 2018) (Figures S6B–S6D; Table S8).

We then searched for the presence of adult stromal cell states in embryonic and neonatal LNs using the label transfer procedure in the "Seurat3" package (Stuart et al., 2019). This strategy allowed us to identify common transcriptional states in different datasets. Transcriptional profiles of clusters from adult LNs were used as reference, and clusters from E17.5 and P2 datasets were putatively assigned to the adult cell state (Figure 7A). Of note, at the embryonic stage, we found that $Cd34^+Ly6a^+Igfbp6^+$ cluster 3 transcriptionally corresponded to adult $Cd34^+Cd248^+$ and $Cd34^+Krt19^+Msln^+$ clusters (Figures 7A and S6A). We also found that the $Acta2^+Myl9^+$ MuC cluster 5 corresponded to the perivascular cell (PvC) Mgp^+ cluster identified in the adult dataset, rather than the $Acta2^+$ and $Rgs5^+$ MuC subpopulations. Intriguingly, the adult PvC Mgp^+ cluster also labeled $Cd34^+$ proliferating precursors at E17.5, suggesting that the adult PvC Mgp^+ cluster may contain $Cd34^+$ progenitors (Figures 7B and S6B).

At the neonatal stage, we identified three clusters (4, 5, and 6) of MuC that appeared to correspond to the respective adult PvC $Acta2^+$ and $Rgs5^+$ PvC subpopulations, whereas the adult PvC Mgp^+ cluster transcriptionally resembled the neonatal MuC $Actg2^+$ and the $Cd34^+$ clusters 0, 1, 2, and 3, likely representing the neonatal stage of embryonic progenitors (Figures 7A and S6B).

Embryonic $Cxcl13^+Isg15^+Bst2^+$ cluster 9 was transcriptionally equivalent to the mature TRC $Ccl19^{high}$ cluster, whereas $Cxcl13^+top2a^+$ cluster 7 and $Cxcl13^+Ccl19^+$ cluster 8 were more similar to the adult Nr4a1 population (Figures 7A and S7A). At the neonatal stage, $Cxcl13^+Cxcl12^+Agtr2^+$ cluster 10 resembled the adult Nr4a1 population, whereas $Cxcl13^+Ccl19^+Clu^+$ was more consistent with all mature TRC clusters (Figures 7A and S7).

To better highlight the dynamic changes in stromal cell distribution across developmental stages, we constructed alluvial plots that clearly show that the $Cd34^+$ cell pool decreases sharply from E17.5 to adult LNs. The latter still contains a small population of $Cd34^+$ cells that may represent a reservoir of progenitor cells, as described previously (Sitnik et al., 2016). In contrast, the pool of $Cxcl13^+$ stromal cells increases and forms more mature subsets (Figure 7B). In conclusion, our findings revealed the existence of $Cd34^+$ and $Cxcl13^+$ proliferating progenitors from which more mature $Cd34^+$, PvC, and Cxcl13 cells originate.

DISCUSSION

Lymphoid stromal cells are crucial organizers of lymphoid compartments and regulators of immune responses. Nevertheless, the embryonic origin, lineage diversity, and transcriptional identity of stromal progenitor cells are largely unknown. We investigated these questions using lineage-tracing approaches in conjunction with scRNA-seq analyses of different LNs along the body axis and at different developmental stages. We used an inducible *Hoxb6CreER*^{T} allele to spatially and temporally label and trace the fate of E8.5 descendants from LPM precursors throughout LN development. Our results showed that LPM descendants contribute to the embryonic and adult stromal cells of all superficial and mesenteric LNs examined, with the exception of cells in cervical LNs, which are known to originate from neural crest cells (Foster et al., 2008). Remarkably, the LPM is the only embryonic mesodermal source of LN stromal cells, as we observed no contribution of the PXM to the stromal cell pool of the superficial and mesenteric LNs. Another exception was the cervical LNs, which arise from neural crest cells that also express *Pax3* (Betancur et al., 2010).

The finding that $Isl1^+$ progenitors give rise to all major stromal cell subsets in the mesenteric and popliteal LNs, but not in other LNs, and the notion that *Isl1* is expressed in a subset of the LPM suggests the existence of other LN-specific lineages within the LPM that contribute to the stromal cell pool. This is supported by a previous observation showing that Fap^+ progenitor cells specifically generate FRCs in mesenteric LN (Denton et al., 2019). Of note, knockout of LTβR signaling in the $Isl1^+$ lineage halts popliteal LN development and causes severe hypoplasia of the mesenteric LN, a phenotype previously observed in LTβR knockout mice (Fütterer et al., 1998). However, T and B cell organization was relatively normal in mutant mice, suggesting that LTβR signaling in Isl1-derived stromal cells is dispensable for lymphocyte organization in the mesenteric LN. Consistent with Isl1 lineages selectively contributing to mesenteric and popliteal LNs, brachial and inguinal LNs were not affected by loss of LTβR signaling through Isl1Cre. In line with previous findings showing the contribution of the Isl1 lineage to splenic stromal cells, loss of LTβR signaling severely affected splenic T and B cell organizations and splenic FDC networks. This confirms the functional role of Isl1 lineage and LTβR signaling in the development of secondary lymphoid organs. The presence of unique LN-specific lineages for stromal cells is also consistent with previous findings showing that $Nkx2.5^+$ progenitors of LPM contribute to the spleen but not to LN stromal cells (Castagnaro et al., 2013). Interestingly, previous work has also shown that stromal cells in the inguinal LNs derive, at least in part, from adipocyte progenitors (Bénézech et al., 2012), a cell

Figure 5. Transcriptional differences across LN and developmental stages

(A) UMAP plot of merged brLN, iLN, and mLN cells in E17.5 and P2 datasets showing stromal ($CD34^+$ SC, $Cxcl13^+$ SC) and mural (MuC) clusters segregation. Each point is a single cell colored by sample of origin (left) or cell type (right).

(B) Violin plots of CD34, CXCL13, and Acta2 gene expression in cell clusters.

(C) Bar graph shows cumulative fractions of cell type clusters in brLN, iLN, and mLNs.

(D and E) Heat map of expression of the top 25 marker genes for individual clusters across LN districts from E17.5 (D) and P2 (E) datasets. Log-normalized expression scaled for each gene. Top 25 marker genes are labeled on the left, and cluster name and district are displayed.

brLN, brachial LN; iLN, inguinal LN; mLN, mesenteric LN.

See also Figure S4 and Tables S1 and S2.

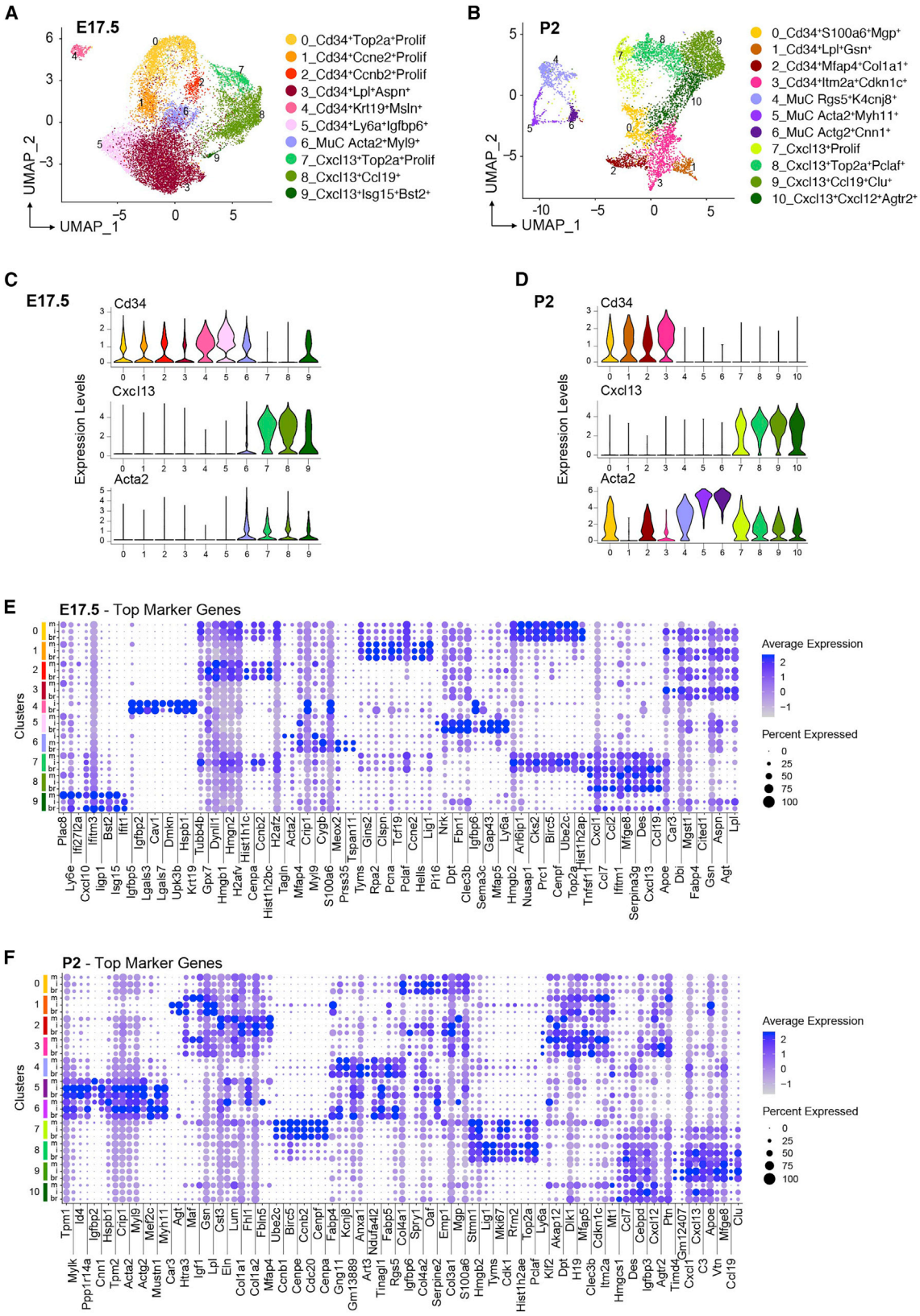
A
E17.5
UMAP_1
UMAP_2
0_Cd34+Top2a+Prolif
1_Cd34+Ccne2+Prolif
2_Cd34+Ccnb2+Prolif
3_Cd34+Lpl+Aspn+
4_Cd34+Krt19+Msln+
5_Cd34+Ly6a+Igfbp6+
6_MuC Acta2+Myl9+
7_Cxcl13+Top2a+Prolif
8_Cxcl13+Ccl19+
9_Cxcl13+Isg15+Bst2+
B
P2
0_Cd34+S100a6+Mgp+
1_Cd34+Lpl+Gsn+
2_Cd34+Mfap4+Col1a1+
3_Cd34+Itm2a+Cdkn1c+
4_MuC Rgs5+K4cnj8+
5_MuC Acta2+Myh11+
6_MuC Actg2+Cnn1+
7_Cxcl13+Prolif
8_Cxcl13+Top2a+Pclaf+
9_Cxcl13+Ccl19+Clu+
10_Cxcl13+Cxcl12+Agtr2+
C
E17.5
Cd34
Cxcl13
Acta2
Expression Levels
D
P2
Cd34
Cxcl13
Acta2
Expression Levels
E
E17.5 - Top Marker Genes
Clusters
Average Expression
Percent Expressed
F
P2 - Top Marker Genes
Clusters
Average Expression
Percent Expressed

type recently shown to arise from E8.5 Hoxb6$^+$ progeny of LPM (Sebo et al., 2018). Thus, LPM is the earliest embryonic source of stromal progenitor cells and contains distinct lineages, such as Nestin$^+$, Fap$^+$, and Isl1$^+$ cell populations, with unique LN contributions. *Isl1* is expressed at E8.5 in the LPM-derived cells (Yang et al., 2006) and later in the splanchnic mesoderm, a derivative of LPM, from which the mesenteric stromal progenitors likely originate (Han et al., 2020). Consistent with the fate-mapping results, our data also showed that *Isl1* mRNA is expressed in the embryonic mesenteric LN, although we did not detect ISL1 protein at early stages of LN development.

Our results also shed light on the embryonic origin of LECs and BECs, which was not addressed in previous fate-mapping analyses. Although the Pax3Cre allele used to mark PXM in our studies is not an inducible model, the data obtained clearly show that embryonic precursors of PXM generate LECs. The only exception we found was LECs in mesenteric LNs derived from the LPM, as shown by the Hoxb6$^+$ and Isl1$^+$ progeny contributing to LECs in this region. Although the vast majority of BECs were not marked by PXM, we noted that rare PNAD$^+$ HEVs derived from Pax3-descendants only brachial and inguinal LNs, and although this contribution was modest, it may reflect the venous origin of LECs (Gutierrez-Miranda and Yaniv, 2020).

The LPM also appears to generate a large proportion of BECs in most LNs, with the PXM making only a modest contribution to axillary (10%) and brachial (20%) BECs. This result is consistent with previous data showing that vascular endothelial cells can arise from both LPM and PXM (Hutcheson et al., 2009; Mayeuf-Louchart et al., 2014; Stone and Stainier, 2019; Wasteson et al., 2008). However, since not all BECs have been labeled by LPM (Hoxb6$^+$ and Isl1$^+$ lineages), it is possible that other lineages contribute to the formation of this cell type. This possibility is supported by recent evidence that BECs can also arise from yolk sac cells that were not labeled with our Cre lines (Plein et al., 2018). Also, the notion that the liver endoderm can also give rise to vascular endothelial cells suggests that there are multiple lineages that give rise BECs (Goldman et al., 2014).

To elucidate the cellular and molecular compositions of mesodermal progenitors in different LNs, we performed scRNA-seq analyses, focusing on nonendothelial cells. At lower resolution, we identified three major populations of stromal cells expressing *Cd34*, *Cxcl13*, and *Acta2* present at embryonic and neonatal stages. Remarkably, the Cd34$^+$ population was more prominent at embryonic stages, whereas the Cxcl13$^+$ population was more prevalent in postnatal stages and beyond. However, this difference may also be due to possible differences based on the cells used for the analysis (embryonic IV^{hi} LTo versus postnatal CD45$^-$). Analysis of gene expression of individual populations in different LNs and developmental stages revealed that there are transcriptomic differences between mesenteric and superficial (inguinal and brachial) LNs, whereas no significant differences were observed between brachial and inguinal LNs. These differences were highlighted by the contribution of *Isl1* expressing lineages to mesenteric but not to superficial LNs and likely reflect the transcriptional identity of each LN along the body axis. Differential expression of Hox transcription factors has also been shown to reflect positional identity of cells during skeletal development (Zakany and Duboule, 2007). In addition, it is also possible that LN-specific signals activate unique transcriptional networks that lead to lineage heterogeneity.

We addressed the question of whether stromal diversity is due to diversification of a homogeneous population or whether there are multiple subsets of stromal cells in embryonic LNs. Interestingly, at higher resolution and after the identification of stromal cell populations across developmental stages, our results showed that LNs at E17.5 comprise multiple clusters of Cd34$^+$ and Cxcl13$^+$ cells. The presence of multiple clusters suggests that the acquisition of stromal diversity begins during embryonic LN development. Although it was not possible to precisely localize each individual cluster, we validated several cluster-specific markers showing their distribution in the embryonic and neonatal LNs. Our scRNA-seq analysis revealed that proliferating clusters are predominantly present in embryonic and postnatal stages in Cd34$^+$ and Cxcl13$^+$ cells, respectively. We hypothesize that these cells may represent the amplifying populations for more differentiated cells in the postnatal LNs. Of note, the observed differences in the proportion of proliferating clusters in the different LNs may be due to differences in tissue growth between mesenteric and superficial LNs, as previously reported (Mebius, 2003). Notably, our analysis cannot completely rule out the possibility that one of the two populations represents the origin of all stromal cells, as isolation of stromal precursors upstream of E17.5 is required to unambiguously resolve this issue.

We also inferred developmental trajectories between stromal cell clusters using the label transfer approach, a computational method that allows cell state classifications to be transferred across embryonic, neonatal, and adult datasets. Interestingly, this approach revealed the presence of transcriptional similarities between adult Cd34$^+$ and Cxcl13$^+$ clusters and their embryonic and neonatal counterparts, indicating a relationship between embryonic Cd34$^+$ proliferating clusters and adult Cd34$^+$ and MuC populations. Our label transfer analysis also revealed the presence of transcriptional similarities between TRC and Nr4a1 subclusters and their embryonic and neonatal Cxcl13$^+$ counterparts. Of note, Cxcl13$^+$ proliferating cells were present in embryonic and neonatal stages but were not found in adult LNs. Nevertheless, our results clearly show that the size of the Cd34$^+$ population decreases, whereas the size of Cxcl13$^+$ cells increases during LN development, and we speculate that proliferating Cxcl13$^+$ cells in embryonic and neonatal LNs may serve as precursors for more differentiated cells.

In conclusion, our work identifies the earliest embryonic source of LN stromal and endothelial cells and indicates that stromal diversity arises during embryonic LN development.

Figure 6. Embryonic LNs contain multiple clusters of Cd34$^+$ and Cxcl13$^+$ stromal cells

(A and B) UMAP plots of merged brLN, iLN, and mLN cells at E17.5 (A) and P2 (B) after applying unbiased clustering at higher resolution.

(C and D) Violin Plots of Cd34, Cxcl13, and Acta2 gene expression in the E17.5 (C) and in the P2 (D) unbiased cell clusters.

(E and F) DotPlot of 10 DEGs per cluster in stromal cells at E17.5 (E) and P2 (F) LNs. Averaged log-normalized expression of the top 10 gene markers for the 10 stromal cell types conserved across LN samples.

See also Figure S5 and Tables S6 and S7.

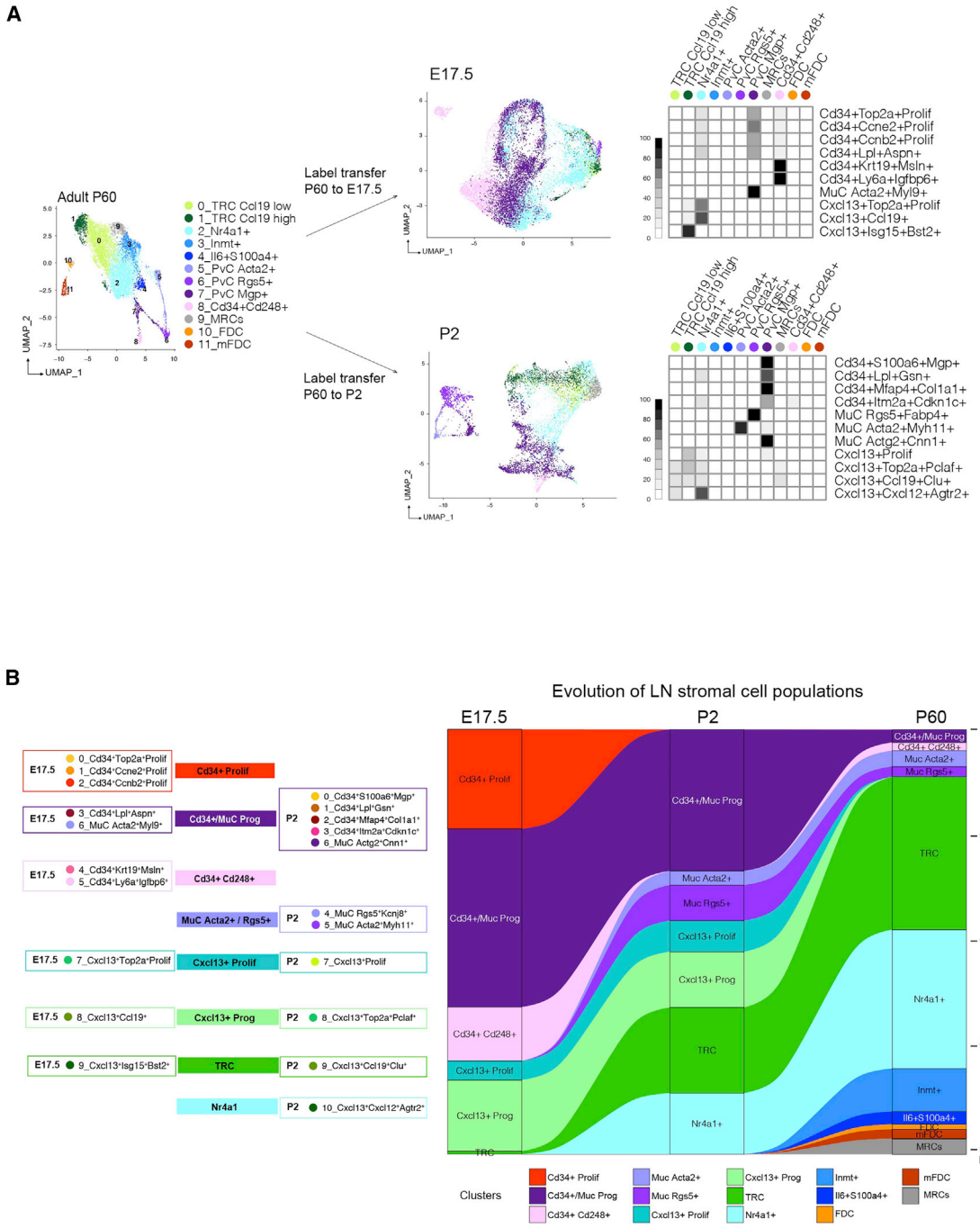

Figure 7. Transcriptional similarities of stromal cell clusters across developmental stages

(A) UMAP plots of LN stromal cells populations from adult (P60) and label transferred to E17.5 and to P2. Heat map representing the percentage of cells labeled as P60 (adult) cell populations for each cell clusters at E17.5 (upper) and P2 (lower).

(B) Sankey diagram showing the evolving differentiation process of each subtype during developmental stages from E17.5 to P2 and then to P60.

See also Figures S6 and S7.

As it is currently possible to generate LPM and PXM precursors from induced pluripotent stem (iPS) cells (Matsuda et al., 2020; Nazareth et al., 2013; Tani et al., 2021), we envisage the possibility of using iPS cells as a source of stromal progenitors to further investigate the molecular factors involved in stromal cell fate decision and, more generally, in lymphoid stromagenesis. Given the critical role of stromal and endothelial progenitor cells in the organization of the lymphoid compartment, we hypothesize that iPS-derived stromal progenitor cells could be used in the context of immune engineering for the development

of functional artificial lympho-organoids to replace LN and restore lymphoid and immunological functions in various diseases in which LN has been resected or dysfunctional, such as cancer, infections, and lymphedema (Dijkstra et al., 2018; Kim et al., 2019; Kobayashi and Watanabe, 2016; Lenti et al., 2019).

Limitations of the study

Our fate-mapping studies revealed that most stromal cells and BECs originate from the embryonic 8.5 mesoderm. However, since a fraction of cells were not labeled by our strategy, it remains to be determined whether recombination at earlier stages is require to label all cells or whether additional mesodermal lineages not expressing *Hoxb6* contribute to generate these cells. Although we showed that embryonic LNs contain multiple clusters of $Cd34^+$ and $Cxcl13^+$ cells transcriptionally related to the adult stromal cell subsets, we were unable to determine precise developmental trajectories as this would require to perform scRNA sequencing of numerous embryonic and postnatal time points.

STAR★METHODS

Detailed methods are provided in the online version of this paper and include the following:

- KEY RESOURCES TABLE
- RESOURCE AVAILABILITY
  - Lead contact
  - Materials availability
  - Data and code availability
- EXPERIMENTAL MODEL AND SUBJECT DETAILS
  - Mice
- METHOD DETAILS
  - Mice irradiation and reconstitution
  - Immunofluorescence staining and confocal analysis
  - Gross morphology
  - Sample preparation and flow cytometry
  - Droplet-based single-cell RNA-seq analysis
  - Unsupervised clustering of scRNA-seq data
  - Integration analysis of stromal subsets
  - Label transfer procedure
  - Statistical analysis

ACKNOWLEDGMENTS

The authors are grateful to the lab members for technical assistance and helpful suggestions. We are grateful to Susan Mackem for providing the *Hoxb6-CreER^T* mice. This work was supported by fundings from Italian Association for Cancer Research (AIRC) grants IG# 14511 and 19867 to A.B., BSF-NSF 2020611 to I.H., and NIH to S.M.E.

and adult LNs; S.B.S., A.M., and J.M.G.-M. performed scRNA-seq data analysis and interpretation of results; F.B., S.B., S.M.E., G.S., N.G.-C., F.B., K.P., T.H., I.H., and V.R. provided reagents, conceptual support, and helped with data interpretation and analyses; E.L., S.B., and A.B. analyzed data, prepared figures, and wrote the manuscript; and A.B. directed the study.

DECLARATION OF INTERESTS

The authors declare no competing interests.

Received: August 4, 2020
Revised: September 30, 2021
Accepted: March 3, 2022
Published: March 30, 2022

REFERENCES

Acton, S.E., Astarita, J.L., Malhotra, D., Lukacs-Kornek, V., Franz, B., Hess, P.R., Jakus, Z., Kuligowski, M., Fletcher, A.L., Elpek, K.G., et al. (2012). Podoplanin-rich stromal networks induce dendritic cell motility via activation of the C-type lectin receptor CLEC-2. Immunity *37*, 276–289.

Bajénoff, M., Egen, J.G., Koo, L.Y., Laugier, J.P., Brau, F., Glaichenhaus, N., and Germain, R.N. (2006). Stromal cell networks regulate lymphocyte entry, migration, and territoriality in lymph nodes. Immunity *25*, 989–1001.

Bénézech, C., Mader, E., Desanti, G., Khan, M., Nakamura, K., White, A., Ware, C.F., Anderson, G., and Caamaño, J.H. (2012). Lymphotoxin-beta receptor signaling through NF-kappaB2-RelB pathway reprograms adipocyte precursors as lymph node stromal cells. Immunity *37*, 721–734.

Bénézech, C., White, A., Mader, E., Serre, K., Parnell, S., Pfeffer, K., Ware, C.F., Anderson, G., and Caamaño, J.H. (2010). Ontogeny of stromal organizer cells during lymph node development. J. Immunol. *184*, 4521–4530.

Betancur, P., Bronner-Fraser, M., and Sauka-Spengler, T. (2010). Assembling neural crest regulatory circuits into a gene regulatory network. Annu. Rev. Cell Dev. Biol. *26*, 581–603.

Bovay, E., Sabine, A., Prat-Luri, B., Kim, S., Son, K., Willrodt, A.H., Olsson, C., Halin, C., Kiefer, F., Betsholtz, C., et al. (2018). Multiple roles of lymphatic vessels in peripheral lymph node development. J. Exp. Med. *215*, 2760–2777.

Brown, F.D., Sen, D.R., LaFleur, M.W., Godec, J., Lukacs-Kornek, V., Schildberg, F.A., Kim, H.J., Yates, K.B., Ricoult, S.J.H., Bi, K., et al. (2019). Fibroblastic reticular cells enhance T cell metabolism and survival via epigenetic remodeling. Nat. Immunol. *20*, 1668–1680.

Buckingham, M., and Rigby, P.W.J. (2014). Gene regulatory networks and transcriptional mechanisms that control myogenesis. Dev. Cell *28*, 225–238.

Buckley, C.D., Barone, F., Nayar, S., Bénézech, C., and Caamaño, J. (2015). Stromal cells in chronic inflammation and tertiary lymphoid organ formation. Annu. Rev. Immunol. *33*, 715–745.

Butler, A., Hoffman, P., Smibert, P., Papalexi, E., and Satija, R. (2018). Integrating single-cell transcriptomic data across different conditions, technologies, and species. Nat. Biotechnol. *36*, 411–420.

Camara, A., Cordeiro, O.G., Alloush, F., Sponsel, J., Chypre, M., Onder, L., Asano, K., Tanaka, M., Yagita, H., Ludewig, B., et al. (2019). Lymph node mesenchymal and endothelial stromal cells cooperate via the RANK-RANKL cytokine axis to shape the sinusoidal macrophage niche. Immunity *50*, 1467–1481.e6.

Castagnaro, L., Lenti, E., Maruzzelli, S., Spinardi, L., Migliori, E., Farinello, D., Sitia, G., Harrelson, Z., Evans, S.M., Guidotti, L.G., et al. (2013). Nkx2-5(+) islet1(+) mesenchymal precursors generate distinct spleen stromal cell subsets and participate in restoring stromal network integrity. Immunity *38*, 782–791.

Cording, S., Wahl, B., Kulkarni, D., Chopra, H., Pezoldt, J., Buettner, M., Dummer, A., Hadis, U., Heimesaat, M., Bereswill, S., et al. (2014). The intestinal micro-environment imprints stromal cells to promote efficient Treg induction in gut-draining lymph nodes. Mucosal Immunol. *7*, 359–368.

Denton, A.E., Carr, E.J., Magiera, L.P., Watts, A.J.B., and Fearon, D.T. (2019). Embryonic FAP(+) lymphoid tissue organizer cells generate the reticular network of adult lymph nodes. J. Exp. Med. *216*, 2242–2252.

Dijkstra, K.K., Cattaneo, C.M., Weeber, F., Chalabi, M., van de Haar, J., Fanchi, L.F., Slagter, M., van der Velden, D.L., Kaing, S., Kelderman, S., et al. (2018). Generation of tumor-reactive T cells by co-culture of peripheral blood lymphocytes and tumor organoids. Cell *174*, 1586–1598.e12.

Dobin, A., Davis, C.A., Schlesinger, F., Drenkow, J., Zaleski, C., Jha, S., Batut, P., Chaisson, M., and Gingeras, T.R. (2013). STAR: ultrafast universal RNA-seq aligner. Bioinformatics *29*, 15–21.

Engleka, K.A., Gitler, A.D., Zhang, M.Z., Zhou, D.D., High, F.A., and Epstein, J.A. (2005). Insertion of Cre into the Pax3 locus creates a new allele of Splotch and identifies unexpected Pax3 derivatives. Dev. Biol. *280*, 396–406.

Fletcher, A.L., Malhotra, D., and Turley, S.J. (2011). Lymph node stroma broaden the peripheral tolerance paradigm. Trends Immunol. *32*, 12–18.

Foster, K., Sheridan, J., Veiga-Fernandes, H., Roderick, K., Pachnis, V., Adams, R., Blackburn, C., Kioussis, D., and Coles, M. (2008). Contribution of neural crest-derived cells in the embryonic and adult thymus. J. Immunol. *180*, 3183–3189.

Fütterer, A., Mink, K., Luz, A., Kosco-Vilbois, M.H., and Pfeffer, K. (1998). The lymphotoxin beta receptor controls organogenesis and affinity maturation in peripheral lymphoid tissues. Immunity *9*, 59–70.

Goldman, O., Han, S.Y., Hamou, W., Jodon de Villeroche, V.J., Uzan, G., Lickert, H., and Gouon-Evans, V. (2014). Endoderm generates endothelial cells during liver development. Stem Cell Rep. *3*, 556–565.

Gutierrez-Miranda, L., and Yaniv, K. (2020). Cellular origins of the lymphatic endothelium: implications for cancer lymphangiogenesis. Front. Physiol. *11*, 577584.

Han, L., Chaturvedi, P., Kishimoto, K., Koike, H., Nasr, T., Iwasawa, K., Giesbrecht, K., Witcher, P.C., Eicher, A., Haines, L., et al. (2020). Single cell transcriptomics identifies a signaling network coordinating endoderm and mesoderm diversification during foregut organogenesis. Nat. Commun. *11*, 4158.

Hutcheson, D.A., Zhao, J., Merrell, A., Haldar, M., and Kardon, G. (2009). Embryonic and fetal limb myogenic cells are derived from developmentally distinct progenitors and have different requirements for beta-catenin. Genes Dev. *23*, 997–1013.

Jarjour, M., Jorquera, A., Mondor, I., Wienert, S., Narang, P., Coles, M.C., Klauschen, F., and Bajénoff, M. (2014). Fate mapping reveals origin and dynamics of lymph node follicular dendritic cells. J. Exp. Med. *211*, 1109–1122.

Kim, S., Shah, S.B., Graney, P.L., and Singh, A. (2019). Multiscale engineering of immune cells and lymphoid organs. Nat. Rev. Mater. *4*, 355–378.

Kiselev, V.Y., Yiu, A., and Hemberg, M. (2018). scmap: projection of single-cell RNA-seq data across data sets. Nat. Methods *15*, 359–362.

Kobayashi, Y., and Watanabe, T. (2016). Gel-trapped Lymphorganogenic chemokines trigger artificial tertiary lymphoid organs and mount adaptive immune responses *in vivo*. Front. Immunol. *7*, 316.

Koning, J.J., Konijn, T., Lakeman, K.A., O'Toole, T., Kenswil, K.J., Raaijmakers, M.H., Michurina, T.V., Enikolopov, G., and Mebius, R.E. (2016). Nestin-expressing precursors give rise to both endothelial as well as nonendothelial lymph node stromal cells. J. Immunol. *197*, 2686–2694.

Koning, J.J., and Mebius, R.E. (2020). Stromal cells and immune cells involved in formation of lymph nodes and their niches. Curr. Opin. Immunol. *64*, 20–25.

Lenti, E., Bianchessi, S., Proulx, S.T., Palano, M.T., Genovese, L., Raccosta, L., Spinelli, A., Drago, D., Andolfo, A., Alfano, M., et al. (2019). Therapeutic regeneration of lymphatic and immune cell functions upon Lympho-organoid transplantation. Stem Cell Rep. *12*, 1260–1268.

Lenti, E., Farinello, D., Yokoyama, K.K., Penkov, D., Castagnaro, L., Lavorgna, G., Wuputra, K., Sandell, L.L., Tjaden, N.E., Bernassola, F., et al. (2016). Transcription factor TLX1 controls retinoic acid signaling to ensure spleen development. J. Clin. Invest. *126*, 2452–2464.

Li, H., Handsaker, B., Wysoker, A., Fennell, T., Ruan, J., Homer, N., Marth, G., Abecasis, G., and Durbin, R.; 1000 Genome Project Data Processing Subgroup (2009). The sequence alignment/map format and SAMtools. Bioinformatics *25*, 2078–2079.

Liao, Y., Smyth, G.K., and Shi, W. (2014). featureCounts: an efficient general purpose program for assigning sequence reads to genomic features. Bioinformatics *30*, 923–930.

Madisen, L., Zwingman, T.A., Sunkin, S.M., Oh, S.W., Zariwala, H.A., Gu, H., Ng, L.L., Palmiter, R.D., Hawrylycz, M.J., Jones, A.R., et al. (2010). A robust and high-throughput Cre reporting and characterization system for the whole mouse brain. Nat. Neurosci. *13*, 133–140.

Martinez, V.G., Pankova, V., Krasny, L., Singh, T., Makris, S., White, I.J., Benjamin, A.C., Dertschnig, S., Horsnell, H.L., Kriston-Vizi, J., et al. (2019). Fibroblastic reticular cells control conduit matrix deposition during lymph node expansion. Cell Rep. *29*, 2810–2822.e5.

Matsuda, M., Yamanaka, Y., Uemura, M., Osawa, M., Saito, M.K., Nagahashi, A., Nishio, M., Guo, L., Ikegawa, S., Sakurai, S., et al. (2020). Recapitulating the human segmentation clock with pluripotent stem cells. Nature *580*, 124–129.

Mayeuf-Louchart, A., Lagha, M., Danckaert, A., Rocancourt, D., Relaix, F., Vincent, S.D., and Buckingham, M. (2014). Notch regulation of myogenic versus endothelial fates of cells that migrate from the somite to the limb. Proc. Natl. Acad. Sci. USA *111*, 8844–8849.

Mebius, R.E. (2003). Organogenesis of lymphoid tissues. Nat. Rev. Immunol. *3*, 292–303.

Muhl, L., Genové, G., Leptidis, S., Liu, J., He, L., Mocci, G., Sun, Y., Gustafsson, S., Buyandelger, B., Chivukula, I.V., et al. (2020). Single-cell analysis uncovers fibroblast heterogeneity and criteria for fibroblast and mural cell identification and discrimination. Nat. Commun. *11*, 3953.

Nazareth, E.J.P., Ostblom, J.E.E., Lücker, P.B., Shukla, S., Alvarez, M.M., Oh, S.K.W., Yin, T., and Zandstra, P.W. (2013). High-throughput fingerprinting of human pluripotent stem cell fate responses and lineage bias. Nat. Methods *10*, 1225–1231.

Nguyen, M.T., Zhu, J., Nakamura, E., Bao, X., and Mackem, S. (2009). Tamoxifen-dependent, inducible Hoxb6CreERT recombinase function in lateral plate and limb mesoderm, CNS isthmic organizer, posterior trunk neural crest, hindgut, and tailbud. Dev. Dyn. *238*, 467–474.

Onder, L., Danuser, R., Scandella, E., Firner, S., Chai, Q., Hehlgans, T., Stein, J.V., and Ludewig, B. (2013). Endothelial cell-specific lymphotoxin-beta receptor signaling is critical for lymph node and high endothelial venule formation. J. Exp. Med. *210*, 465–473.

Onder, L., Mörbe, U., Pikor, N., Novkovic, M., Cheng, H.W., Hehlgans, T., Pfeffer, K., Becher, B., Waisman, A., Rülicke, T., et al. (2017). Lymphatic endothelial cells control initiation of lymph node organogenesis. Immunity *47*, 80–92.e4.

Perez-Shibayama, C., Gil-Cruz, C., and Ludewig, B. (2019). Fibroblastic reticular cells at the nexus of innate and adaptive immune responses. Immunol. Rev. *289*, 31–41.

Pezoldt, J., Pasztoi, M., Zou, M., Wiechers, C., Beckstette, M., Thierry, G.R., Vafadarnejad, E., Floess, S., Arampatzi, P., Buettner, M., et al. (2018). Neonatally imprinted stromal cell subsets induce tolerogenic dendritic cells in mesenteric lymph nodes. Nat. Commun. *9*, 3903.

Plein, A., Fantin, A., Denti, L., Pollard, J.W., and Ruhrberg, C. (2018). Erythromyeloid progenitors contribute endothelial cells to blood vessels. Nature *562*, 223–228.

Prummel, K.D., Nieuwenhuize, S., and Mosimann, C. (2020). The lateral plate mesoderm. Development *147*, dev175059.

Rodda, L.B., Lu, E., Bennett, M.L., Sokol, C.L., Wang, X., Luther, S.A., Barres, B.A., Luster, A.D., Ye, C.J., and Cyster, J.G. (2018). Single-cell RNA sequencing of lymph node stromal cells reveals niche-associated heterogeneity. Immunity *48*, 1014–1028.e6.

Schaeuble, K., Britschgi, M.R., Scarpellino, L., Favre, S., Xu, Y., Koroleva, E., Lissandrin, T.K.A., Link, A., Matloubian, M., Ware, C.F., et al. (2017). Perivascular fibroblasts of the developing spleen act as LTalpha1beta2-dependent precursors of both T and B zone organizer cells. Cell Rep. *21*, 2500–2514.

Sebo, Z.L., Jeffery, E., Holtrup, B., and Rodeheffer, M.S. (2018). A mesodermal fate map for adipose tissue. Development *145*, dev166801.

Sitnik, K.M., Wendland, K., Weishaupt, H., Uronen-Hansson, H., White, A.J., Anderson, G., Kotarsky, K., and Agace, W.W. (2016). Context-dependent development of lymphoid stroma from adult CD34(+) adventitial progenitors. Cell Rep. *14*, 2375–2388.

Sixt, M., Kanazawa, N., Selg, M., Samson, T., Roos, G., Reinhardt, D.P., Pabst, R., Lutz, M.B., and Sorokin, L. (2005). The conduit system transports soluble antigens from the afferent lymph to resident dendritic cells in the T cell area of the lymph node. Immunity *22*, 19–29.

Smith, T., Heger, A., and Sudbery, I. (2017). UMI-tools: modeling sequencing errors in unique molecular identifiers to improve quantification accuracy. Genome Res. *27*, 491–499.

Srinivas, S., Watanabe, T., Lin, C.S., William, C.M., Tanabe, Y., Jessell, T.M., and Costantini, F. (2001). Cre reporter strains produced by targeted insertion of EYFP and ECFP into the ROSA26 locus. BMC Dev. Biol. *1*, 4.

Stone, O.A., and Stainier, D.Y.R. (2019). Paraxial mesoderm is the major source of lymphatic endothelium. Dev. Cell *50*, 247–255.e3.

Stuart, T., Butler, A., Hoffman, P., Hafemeister, C., Papalexi, E., Mauck, W.M., 3rd, Hao, Y., Stoeckius, M., Smibert, P., and Satija, R. (2019). Comprehensive integration of single-cell data. Cell *177*, 1888–1902.e21.

Sun, Y.F., Liang, X.Q., Najafi, N., Cass, M., Lin, L.Z., Cai, C.L., Chen, J., and Evans, S.M. (2007). Islet 1 is expressed in distinct cardiovascular lineages, including pacemaker and coronary vascular cells. Dev. Biol. *304*, 286–296.

Tani, S., Chung, U.I., Ohba, S., and Hojo, H. (2020). Understanding paraxial mesoderm development and sclerotome specification for skeletal repair. Exp. Mol. Med. *52*, 1166–1177.

Tani, S., Okada, H., Chung, U.I., Ohba, S., and Hojo, H. (2021). The progress of stem cell technology for skeletal regeneration. Int. J. Mol. Sci. *22*, 1404.

Thierry, G.R., Gentek, R., and Bajenoff, M. (2019). Remodeling of reactive lymph nodes: dynamics of stromal cells and underlying chemokine signaling. Immunol. Rev. *289*, 42–61.

Vanlandewijck, M., He, L., Mäe, M.A., Andrae, J., Ando, K., Del Gaudio, F., Nahar, K., Lebouvier, T., Laviña, B., Gouveia, L., et al. (2018). A molecular atlas of cell types and zonation in the brain vasculature. Nature *554*, 475–480.

Wasteson, P., Johansson, B.R., Jukkola, T., Breuer, S., Akyürek, L.M., Partanen, J., and Lindahl, P. (2008). Developmental origin of smooth muscle cells in the descending aorta in mice. Development *135*, 1823–1832.

Wimmer, N., Huber, B., Barabas, N., Röhrl, J., Pfeffer, K., and Hehlgans, T. (2012). Lymphotoxin beta receptor activation on macrophages induces cross-tolerance to TLR4 and TLR9 ligands. J. Immunol. *188*, 3426–3433.

Yang, L., Cai, C.L., Lin, L., Qyang, Y., Chung, C., Monteiro, R.M., Mummery, C.L., Fishman, G.I., Cogen, A., and Evans, S. (2006). Isl1Cre reveals a common Bmp pathway in heart and limb development. Development *133*, 1575–1585.

Zakany, J., and Duboule, D. (2007). The role of Hox genes during vertebrate limb development. Curr. Opin. Genet. Dev. *17*, 359–366.

Zhuang, S.W., Zhang, Q.Q., Zhuang, T., Evans, S.M., Liang, X.Q., and Sun, Y.F. (2013). Expression of Isl1 during mouse development. Gene Expr. Patterns *13*, 407–412.

STAR★METHODS

KEY RESOURCES TABLE

REAGENT or RESOURCE	SOURCE	IDENTIFIER
Antibodies		
Mouse anti-mouse α-SMA (1A4)	Sigma-Aldrich	Cat# A5228 RRID: AB_262054
PE anti-mouse CD3 (145-2C11)	Miltenyi Biotec	Cat# 130-102-792 RRID: AB_2660393
Alexa Fluor 647 anti mouse CD45R/B220 (RA3-6B2)	Thermo Fisher Scientific	Cat# RM2621 RRID: AB_10373821
Goat anti-mouse CCL21/6Ckine	R&D systems	Cat# AF457 RRID: AB_2072083
Rat anti-mouse CD4 (GK1.5)	eBioscience	Cat# 14-0041-86 RRID: AB_467065
APC anti-mouse CD31 (MEC13.3)	Biolegend	Cat# 102510 RRID: AB_312917
PerCP/Cyanine5.5 anti-mouse CD31	Biolegend	Cat# 102522 RRID: AB_2566761
Recombinant rabbit anti-CD34 antibody (EP373Y)	Abcam	Cat# Ab81289 RRID: AB_1640331
Biotin rat anti-mouse CD35 (8C12)	BD Biosciences	Cat# 553816 RRID: AB_395068
BV510 anti-mouse CD35 (8C12)	BD Biosciences	Cat# 740132 RRID: AB_2739889
eFluor 450 anti-mouse CD45 (30-F11),	eBioscience	Cat# 48-0451-82 RRID: AB_1518806
Mouse anti-mouse CD45.2 (104)	Biolegend	Cat# 109802 RRID: AB_313439
APC anti-mouse CD45.2 (104)	Biolegend	Cat# 109814 RRID: AB_389211
APC/Cyanine7 anti-mouse CD45.2	Biolegend	Cat# 109824 RRID: AB_830789
PE/Cyanine7 anti-mouse CD45.2	Biolegend	Cat# 109829 RRID: AB_1186103
Alexa Fluor 488 anti-mouse VCAM1/CD106 (429 (MVCAM.A))	Biolegend	Cat# 105710 RRID: AB_493427
PE/Cyanine7 anti-mouse CD140a (APA5)	Biolegend	Cat# 135911 RRID: AB_2715973
Rabbit anti-mouse Collagen IV	Novus Biologicals	Cat# NB120-6586 RRID: AB_789360
Goat anti-mouse CXCL13/BLC/BCA-1	R&D Systems	Cat# AF470 RRID: AB_355378
PerCP/Cyanine5.5 anti-mouse ICAM/CD54 (YN1/1.7.4)	Biolegend	Cat# 116124 RRID: AB_2715952
Rat anti-Fibroblasts (ER-TR7)	Acris	Cat# BM4018 RRID: AB_981318
Rat anti-Sca1/Ly6A/E (E13 161-7)	Abcam	Cat# Ab51317 RRID: AB_1640946
Rabbit anti-LYVE-1	Novus Biologicals	Cat# NB600-1008 RRID: AB_10000497
Biotin rat anti-mouse MAdCAM-1 antibody (MECA-367)	Biolegend	Cat# 120706 RRID: AB_493397

Continued

REAGENT or RESOURCE	SOURCE	IDENTIFIER
APC anti-mouse MAdCAM-1 (MECA-367)	Biolegend	Cat# 120711 RRID: AB_2629561
Chicken anti mCherry	Novus Biologicals	Cat# NBP2-25158 RRID: AB_2636881
Rat anti-mouse PNAd (MECA-79)	BD Biosciences	Cat# 553863 RRID: AB_395099
Hamster anti-mouse GP38 (8.1.1)	eBioscience	Cat# 14-5381-82 RRID: AB_1210505
APC/Cyanine7 anti-mouse GP38 (8.1.1)	Biolegend	Cat# 127418 RRID: AB_2629804
Secondary antibody		
Biotinylated horse anti-goat IgG	Vector Laboratories	Cat# BA-9500 RRID: AB_2336123
Alexa Fluor 546 goat anti-chicken IgY	Thermo Fisher Scientific	Cat# A-11040 RRID: AB_2534097
Alexa Fluor 568 goat anti-mouse IgG	Thermo Fisher Scientific	Cat# A-11031 RRID: AB_144696
Alexa Fluor 647 donkey anti-rabbit IgG	Thermo Fisher Scientific	Cat# A-31573 RRID: AB_2536183
Alexa Fluor 546 goat anti-rabbit IgG	Thermo Fisher Scientific	Cat# A-11035 RRID: AB_2534093
Biotinylated goat anti-rabbit IgG	Vector Laboratories	Cat# BA-1000 RRID: AB_2313606
Alexa Fluor 647 goat anti-rat IgG	Thermo Fisher Scientific	Cat# A-21247 RRID: AB_141778
Alexa Fluor 546 goat anti-rat IgG	Thermo Fisher Scientific	Cat# A-11081 RRID: AB_2534125
Biotinylated goat anti-rat IgG	Vector Laboratories	Cat# BA-9401 RRID: AB_2336208
Streptavidin-Alexa Fluor 546	Thermo Fisher Scientific	Cat# S-11225 RRID: AB_2532130
Chemicals, peptides, and recombinant proteins		
Tamoxifen	Sigma-Aldrich	Cat# T5648
Progesterone	Sigma-Aldrich	Cat# P0130
Antigenfix	Diapath	Cat# P0014
Killik (O.C.T.)	Bio-Optica	Cat# 05-9801
Dehyol 95	Bio-Optica	Cat# 06-10070Q
Avidin/Biotin Blocking Kit	Vector Laboratories	Cat# SP-2001
M.O.M.® (Mouse on Mouse) Blocking Reagent	Vector Laboratories	Cat# MKB-2213-1
DAPI	Sigma-Aldrich	Cat# 32670
MOWIOL® 4-88 Reagent	Merck	Cat# 475904-M
Collagenase/Dispase	Roche	Cat# 10269638001
Collagenase P	Roche	Cat# 11213857001
DNAse I	Roche	Cat# 11284932001
Liberase	Roche	Cat# 05401119001
Anti-APC MicroBeads	Miltenyi Biotec	Cat# 130-090-855
CD45 MicroBeads, mouse	Miltenyi Biotec	Cat# 130-052-301
MACS LS columns	Miltenyi Biotec	Cat# 130-042-401
MACS MS columns	Miltenyi Biotec	Cat# 130-042-201
Critical commercial assays		
TSA Fluorescein System	Akoya Biosciences	Cat#NEL701A001KT
ChromiumTM Single Cell 3' Library & Gel Bead Kit v2, 16 rxns	10X Genomics	Cat# PN-120237

Continued		
REAGENT or RESOURCE	SOURCE	IDENTIFIER
Chromium Single Cell 3′ Library Kit	10x Genomics	Cat# PN-120234
Chromium Single Cell 3′ Gel Bead Kit	10x Genomics	Cat# PN-120235
Chromium i7 Multiplex Kit	10x Genomics	Cat# PN-120262
Chromium Single Cell A Chip Kit	10x Genomics	Cat# PN-120236
Deposited data		
Single-cell RNaseq data	This manuscript	NCBI Gene Expression Omnibus (GEO) accession GEO: GSE151623
Experimental models: Organisms/strains		
Mouse: *Hoxb6CreER*^{T}	Nguyen et al., 2009	Internal colony
Mouse: *Isl1*$^{Cre/+}$,	Sun et al., 2007	Internal colony
Mouse: *Pax3*$^{Cre/+}$	The Jackson Laboratory	Stock No: 005549
Mouse: *Ltβr*$^{fl/fl}$	Wimmer et al., 2012	Internal colony
Mouse: *Rosa26-tdTomato*	The Jackson Laboratory	Stock No: 007914
Software and algorithms		
Prism 7.0	GraphPad	https://www.graphpad.com/scientific-software/prism
FlowJo V10	TreeStar	https://www.flowjo.com/
ImageJ V1.5	Imagej	N/A
Adobe Illustrator CC 2019	Adobe	N/A
Leica Application Suite X (LAS X)	Leica Microsystem	N/A
Seurat (v3.2.2)	Stuart et al., 2019	https://satijalab.org/seurat/
CellRanger	10x Genomics	https://support.10xgenomics.com/single-cell-gene-expression/software/downloads/latest
Other		
BD FACSCanto II	BD Bioscience	N/A
BD FACSAria III SORP	BD Bioscience	N/A
SP5 or SP8 confocal microscope	Leica Microsystem	N/A
Stereo Microscope Stemi 508	Zeiss	N/A
AxioCam ERc 5s	Zeiss	N/A
Illumina Novaseq 6000 system	Illumina	N/A

RESOURCE AVAILABILITY

Lead contact

Further information and requests for resources should be directed to and will be fulfilled by the lead contact, Andrea Brendolan (brendolan.andrea@hsr.it).

Materials availability

This study did not generate new unique reagents. The authors declare that all the results supporting the findings of this study are available within the paper and its figures.

Data and code availability

Single Cell RNA-seq data generated during this study have been deposited in the Gene Expression Omnibus (GEO) with the accession code GEO: GSE151623. The authors declare that all data supporting the findings of this study are available within the manuscript or its supplemental information or are available from the corresponding author upon request.

EXPERIMENTAL MODEL AND SUBJECT DETAILS

Mice

Hoxb6CreER^{T}, *Isl1*$^{Cre/+}$, *Pax3*$^{Cre/+}$ *and Ltβr*$^{fl/fl}$ mice have been previously described (Nguyen et al., 2009; Sun et al., 2007; Yang et al., 2006; Wimmer et al., 2012). Rosa26-tdTomato mice were used as a reporter strain to evaluate Cre activity (Madisen et al., 2010).

8-12 weeks-old female mice were used in the experiments. Animals were bred and maintained in a specific pathogen-free animal facility with a 12-hour light/12-hour dark cycle, at 18–23 °C with 40–60% humidity under barrier conditions. All animal care were in compliance with the Guide for the Care and Use of Laboratory Animals published by the US National Institutes of Health, as well as institutional guidelines at the University of California, San Diego and Silberman Institute of Life Sciences, Jerusalem; and in accordance with European Union and San Raffaele Scientific Institute Institutional Animal Care and Use Committee (IACUC) guidelines.

METHOD DETAILS

Mice irradiation and reconstitution

For the induction of the CreER^{T} recombinase, pregnant mice at embryonic stage E8.5 received via oral gavage a single dose of Tamoxifen and Progesterone (200 μl/mouse of 10mg/ml tamoxifen with 5mg/ml progesterone in corn oil) (#T5648 and #P0130, Sigma-Aldrich). For embryonic staging, detection of vaginal plug was designated as E0.5. For the generation of chimeras, eight-weeks old Hoxb6CreER^{T};R26tdTomato and Islet1$^{Cre/+}$;R26tdTomato mice were lethally irradiated by exposure to two cycles of 5,4Gy (3-hour interval) from a cesium radiation source, and the day after mice were reconstituted with 1x10^{7} C57BL/6N total bone marrow cells by intravenous injection into the tail vein.

Immunofluorescence staining and confocal analysis

Embryonic, neonatal and adult tissues were harvested and fixed for 5 minutes in AntigenFix (# P0014, Diapath), then washed in PBS 1X and dehydrated overnight in 30% sucrose (Sigma-Aldrich) at 4°C. Samples were embedded in Killik O.C.T. (#05-9801, Bio-optica) and frozen in ethanol dry-ice bath (using Dehyol 95 (#05-9801, Bio-optica). 6-8 μm thick sections were prepared using a cryostat and placed onto glass slides (SuperFrost® Plus, Thermo Fisher Scientific), fixed in cold acetone for 5 minutes, dried, and kept at -80°C until used. Slides were hydrated and blocked for 30 min with blocking buffer (PBS1X, 0.5% FBS, 0.05% Tween20) at room temperature (RT) followed by 1 hour incubation at RT with the following primary antibodies: anti-α-SMA (#A5228,Sigma-Aldrich,1:100), anti-CD3PE (#130-102-792, Miltenyi Biotec, 1:200), anti-CD45R/B220 Alexa Fluor 647 (#RM2621, Thermo Fisher Scientific, 1:100), anti-CD4 (#14-0041-86, eBioscience, 1:50), anti-CD31 APC (#102510, Biolegend, 1:200), anti-CD35 (#553816, BD Biosciences, 1:100), anti-CD45 e-Fluor 450 (#48-0451-82, eBioscience, 1:50), anti-CD45.2 (#109802, Biolegend, 1:200), anti-Collagen IV (#NB120-6586, Novus Biologicals, 1:500), anti-ER-TR7 (#BM4018, Acris, 1:500), anti-Lyve-1 (#NB600-1008, Novus Biologicals, 1:500), anti-mCherry (#NBP2-25158, Novus Biologicals, 1:2000), anti-PNAd (#553863, BD Biosciences, 1:500). Slides were washed and incubated 30 min at RT with the following secondary reagents: Alexa Fluor 546- conjugated anti-chicken, Alexa Fluor 568-conjugated anti-mouse, Alexa Fluor 546- and Alexa Fluor 647-conjugated anti-rabbit, Streptavidin-Alexa Fluor 546-conjugated, Alexa Fluor 546- and Alexa Fluor 647-conjugated anti-rat (all from Thermo Fisher Scientific, 1:500). Slides were washed and stained with DAPI (#32670, Sigma-Aldrich, 1:500) for 5 min, washed again and mounted with MOWIOL (#475904-M, Merck). For staining with anti-α-SMA antibody an additional 20 min incubation at RT with M.O.M. (#MKB-2213-1, Vector Laboratories) before blocking buffer was performed; instead for staining with anti-CD35 antibody an additional incubation at RT with Avidin/Biotin Blocking Kit (#SP-2001, Vector Laboratories) before blocking buffer was done. Immunofluorescence staining with amplification of signal using TSA Plus fluorescein kit (#NEL701A001KT, AKOYA Biosciences) was used for the following antibodies: anti-CCL21 (#AF457, R&D systems, 1:200), anti-CD34 (#Ab81289, Abcam, 1:2000), anti-CXCL13 (#AF470, R&D Systems, 1:100), anti- Ly6A (#Ab51317, Abcam, 1:5000), anti-MAdCAM-1 (#120706, Biolegend, 1:10.000), anti-GP38 (#14-5381-82, eBioscience, 1:500). Slides were hydrated and incubated at RT with Avidin/Biotin Blocking Kit. Then slides were blocked with AKOYA blocking buffer for 30 min and incubated with primary antibodies for 1 hour at RT. Slides were then washed and incubated 30 min at RT with the appropriate biotinylated secondary antibody (anti-goat IgG, anti-rat IgG, goat anti-rabbit IgG all from Vector Laboratories, 1:500) followed by another 30 min incubation at RT with Streptavidin-horseradish peroxidase conjugate (SA-HRP conjugated, 1:100, from the kit). After washing, to amplify the signal, incubation for 7min with TSA fluorescein was done. Confocal images were acquired using a 40x oil-immersion objective using SP5 or SP8 confocal microscope (Leica Microsystem). Digital images were recorded in separately scanned channels with no overlap in detection of emissions from the respective fluorochromes. Final image processing was performed with ImageJ and Adobe Illustrator.

Gross morphology

Cervical, axillary, brachial, inguinal, mesenteric, popliteal lymph nodes (LNs) and spleens were collected from *Ltβr$^{fl/fl}$, Ltβr$^{fl/+}$;Islet1$^{Cre/+}$ and Ltβr$^{fl/fl}$;Islet1$^{Cre/+}$* female mice at two-months of age. Organs were weighted using an analytical balance (Mettler Toledo) and pictures were acquired using a stereo microscope (Stemi508, Zeiss) equipped with a camera (Axiocam ERc 5s, Zeiss). Inguinal, mesenteric LNs and spleens were then processed for immunofluorescence staining as described above (see Immunofluorescence staining and confocal analysis section).

Sample preparation and flow cytometry

For flow cytometry analysis of stromal populations in adult LNs: cervical, axillary, brachial, inguinal, mesenteric and popliteal LNs were collected from *Islet1$^{Cre/+}$; R26-tdTomato, Hoxb6CreER^{T};R26-tdTomato* and *Pax3$^{Cre/+}$;R26-tdTomato* mice at 2-3 months of age. LNs were enzymatically digested as previously described (Fletcher et al., 2011). In brief, tissues were placed in DMEM containing 2% FBS (Lonza) and 20mM Hepes (Sigma-Aldrich), 0.2 mg/ml Collagenase P (#11213857001, Roche), 100 μg/ml DNase I

(#11284932001, Roche), and 0.8 U/ml Collagenase/Dispase (#10269638001, Roche) and reduced in small pieces using forceps. Tissues were incubated for 30 min at 37°C at 900rpm, using a thermomixer, to facilitate the release of stromal cells. Digested material was collected every 10 min and kept at 4°C in PBS 1X with 1% FBS and 10mM EDTA. Larger fragments were pipetted with fresh digestion mix and replaced into the thermomixer for the remaining time. Hematopoietic cells were depleted by incubating the cell suspension with anti-CD45 APC (#109814, Biolegend) and subsequently with anti-APC microbeads (Miltenyi Biotech #130-090-855) and passing it through MACS LS/MS columns (Miltenyi Biotech #130-042-401/130-042-201). Unbound single-cell suspension, containing stromal and endothelial cells, was blocked for 15 min at RT and after incubated for 10 min at 4°C with the following antibody: anti-CD31 PerCP/Cyanine5.5 (#102522, Biolegend, 1:100), anti-CD35 BV510 (#740132, Biolegend, 1:100), anti-CD140a PE/Cyanine7 (#135911, Biolegend, 1:100), anti-MAdCAM-1 APC (#120711, Biolegend, 1:100), anti-GP38 APC/Cyanine7 (#127418, Biolegend, 1:200).

For flow cytometry analysis of stromal populations in embryonic LNs: inguinal, mesenteric and brachial LNs at embryonic day 17.5 (E17.5) were collected from *Islet1*$^{Cre/+}$*; R26-tdTomato* and *Hoxb6CreER*^{T}*;R26-tdTomato* mice. Embryonic LNs were digested in RPMI containing 2% FBS and 20mM Hepes, 0.8 U/ml Collagenase/Dispase and 100 μg/ml DNAse I with the same steps described above for adult LNs. Single cells suspension was blocked for 15 min at RT and after incubated 10 min at 4°C with the following antibody: anti-CD31 APC (#102510, Biolegend, 1:200), anti-CD45.2 APC/Cyanine7 (#109824, Biolegend, 1:200), anti-CD45.2 PE/Cyanine7 (#109829, Biolegend, 1:200), anti-CD140a PE/Cyanine7 (#135911, Biolegend, 1:100), anti-ICAM-1 PerCP/Cyanine5.5 (#116124, Biolegend, 1:100), anti-MAdCAM-1 APC (#120711, Biolegend, 1:100), anti-GP38 APC/Cyanine7 (#127418, Biolegend, 1:200), anti-VCAM-1 Alexa Fluor 488 (#105710, Biolegend, 1:100). Dead cells were excluded using DAPI (#32670, Sigma-Aldrich, 1:500).

Data were acquired using FACSCanto II (BD Bioscience) and analysed using FlowJo v10.6.2 (TreeStar, Ashland, OR, USA).

Droplet-based single-cell RNA-seq analysis

Droplets-based scRNA-seq was performed on wild-type C57BL6/N LNs stromal cells isolated from brachial (br), inguinal (i) and mesenteric (m) LNs at three different time points: embryonic day 17.5 (E17.5), postnatal day 2 (P2) and at 8-weeks of age (P60). LNs were harvested in RPMI (Fisher Scientific) supplemented with 2% FBS (EuroClone), 20mM HEPES (Fisher Scientific) and kept on ice. Next, tissues were processed following different protocols depending on the developmental stage.

At E17.5, LN were digested using 0.8 U/ml Collagenase/Dispase (Roche) and 100 μg/ml DNAse I (Roche) in RPMI with 2% FBS and 20mM Hepes. Tissues were incubated at 37°C for 30 minutes at 900rpm in the thermomixer. Every 10 minutes, supernatants were transferred into a new tube with MACS buffer and larger fragments were pipetted with fresh digestion mix and replaced into the thermomixer for the remaining time. Pooled digested cell suspensions were centrifuged, cells counted and stained with anti-CD45 (Biolegend), anti-VCAM-1 Alexa Fluor 488 and anti-ICAM-1 PerCP/Cyanine5.5 antibodies for cells sorting using FACSaria III SORP (BD Bioscience) with a 100-micron nozzle and 20 psi. Fifteen thousand of CD45^{-}/I^{hi}/V^{hi} LTo sorted cells from each sample were spun down and immediately run on the 10X Chromium analyzer (10X Genomics).

For P2 LNs, tissues were enzymatically digested with 0.45mg/ml Liberase^{TM} (#05401119001, Roche) in RPMI with 2% FBS and 20mM Hepes for 20 min at 37°C in thermomixer at 900rpm. To enrich stromal cells, hematopoietic cells were depleted by incubating the cell suspension with MACS anti-CD45 microbeads (Miltenyi Biotech #130-052-301), following the manufacturer's protocol, and passing them through MACS MS columns. Ten thousand of enriched CD45 negative stromal cells from each sample were run on the 10X Chromium analyzer (10x Genomics).

Adult (P60) LNs were digested using 0.2mg/ml Collagenase (Roche), 0.45mg/ml Liberase (Roche) and 100μg/ml DNAseI (Roche) in RPMI with 2% FBS and 20mM Hepes. Samples were incubated for 30 minutes at 37°C in the thermomixer at 900rpm, and every 10 minutes, samples were processed as described before. To enrich stromal cells, the hematopoietic fraction was depleted by incubating the cell suspension with anti-CD45 APC antibody and next with MACS anti-APC microbeads (Miltenyi Biotec). Finally, unbound single cell suspension was stained for CD45, CD31 and GP38. Fifteen thousand sorted stromal (CD45^{-}CD31^{-}GP38^{+}) and endothelial (CD45^{-}CD31^{+}GP38^{-} and CD45CD31^{+}GP38^{+}, BEC and LEC respectively) cells from each sample were spun down and immediately run on the 10X Chromium analyzer (10X Genomics).

After the run on the 10X Chromium, all samples were processed for the library preparation, following the manufacture's protocol of the Chromium Single Cell 3' Reagent Kit (v2 Chemistry, 10X Genomics). Libraries were run on the NextSeq 500 or NovaSeq 600 sequencer (Illumina) for sequencing in paired-end mode (2 × 150 cycles). FASTQ files were demultiplexed from raw base call (BCL) files using 10x Genomics 'cellranger demux' (CellRanger v 2.1.1). The P2 samples dataset was processed as follows. The whitelist of cell barcodes was identified with 'umi_tools whitelist –set-cell-number 5000 –bc-pattern=CCCCCCCCCCCCCCCCNNNNNNNNNN' (umi_tools v0.5.4) (Smith et al., 2017). Reads of the whitelisted cells were extracted with 'umi_tools extract –bc-pattern=CCCCCCCCCCCCCCCCNNNNNNNNNN –filter-cell-barcode –whitelist=whitelist.txt' (umi_tools v0.5.4). Extracted reads were aligned with STAR aligner (v2.5.3a) (Dobin et al., 2013) to the primary reference assembly of the mouse genome (mm10/GRCm38) with parameter '–outFilterMultimapNmax 1' (to exclude multi-mapping reads). Mapped reads were assigned to gene_name attributes from GENCODE basic annotation for GRCm38 (version M16) using Subread featureCounts (v1.6.2) (Liao et al., 2014). Results were saved in BAM files with option 'featureCounts -R BAM' and successively sorted and indexed with samtools (v1.4) (Li et al., 2009). Per gene counts were summarized for each cell using 'umi_tools count –per-gene –gene-tag=XT –assigned-status-tag=XS –per-cell –wide-format-cell-counts' (umi_tools v0.5.5). The E17.5 and adult samples datasets were processed using CellRanger (v4.0.0) ''cellranger count'' with the same annotation from GENCODE.

Unsupervised clustering of scRNA-seq data

Raw counts data were further analysed with the Seurat R package (version 2.3.4 for the initial sample merge analysis; version 3.1.1 for the analysis on integrated stromal subsets) (Butler et al., 2018) all functions mentioned are from this package, unless otherwise noted and were used with the default parameters unless otherwise noted. For each sample, we retained only cells (unique barcodes) that expressed at least 200 genes and only genes that were expressed in at least 5 cells. We also excluded cells with more than 10% of reads mapping to mitochondrial genes and cells with more than 7000 genes (upon inspection of their scatter plots in each sample with GenePlot function). For E17.5 dataset, this left us with a total of 18,882 genes across 15,451 cells (2,217 median genes in 5,214 cells in brachial LN, 2,211 median genes in 4915 cells in inguinal LN, 2064 median genes in 5,322 cells in mesenteric LN). For P2 dataset, this left us with a total of 23,766 genes across 11,397 cells (2,033 median genes in 3,489 cells in brachial LN, 2,232 median genes in 4,574 cells in inguinal LN, 2,252 median genes in 3,334 cells in mesenteric LN). For adult dataset, this left us with a total of 18,218 genes across 24,752 cells (977 median genes in 9,583 cells in brachial LN, 1,000 median genes in 10,063 cells from inguinal LN, 635 median genes in 5,106 cells in mesenteric LN). We next applied library-size normalization to each cell with NormalizeData. To reduce the influence of variability in the number of UMIs and mitochondrial gene expression between cells on the clustering, we used the ScaleData function to linearly regress out these sources of variation and to scale and centre the data for dimensionality reduction. For the three datasets, principal component analysis was run using RunPCA on the variable genes calculated with FindVariableGenes (top 2000). The number of principal components to use was decided based on the ElbowPlot (nPCs = 20-30). We ran FindClusters to apply shared nearest neighbour (SNN) graph-based clustering (resolutions were adjusted by visually inspecting UMAP plots). We identified markers for the found clusters with FindAllMarkers (bimodal test(P2) and Wilcoxon.test (E17.5 and adult), min.pct = 0.25, only.pos = TRUE, thresh.use = 0.25). These included known endothelial (*Flt1, Sox17* for BEC; *Lyve1, Prox1* for LEC) and non-endothelial (*Cxcl13, Ccl19, Cd34*) stromal marker genes. For all datasets, we excluded from further analyses clusters expressing non-stromal markers (e.g. myelin genes, CD45 expressing cells), endothelial cells (BEC and LEC clusters), clusters with a median number of expressed genes per cell lower than 500) and cells with more than 50 counts of haemoglobin genes (Hbb-bs, Hba-a1, Hba-a2) as red blood cells (Figure S4A; Table S2). For E17.5, the final stromal cell subset comprised 15,168 cells (5,134 from brLN, 4858 from iLN and 5,176 from mLN). For P2, the final subset comprised 7,468 cells (1859 from brLN, 3552 from iLN and 2057 from mLN). For the adult, the final subset comprised 9,235 cells (3,590 from brLN, 3,830 from iLN and 1,815 from mLN). Uniform Manifold Approximation and Projection (UMAP) was obtained with RunUMAP and plotted with DimPlot.

Integration analysis of stromal subsets

To make sure we were studying the three LN stromal subsets within the same framework, we used Seurat's (v3.1.1) integration approach to harmonize them (Stuart et al., 2019). Initially the three LN districts were integrated in E17.5, P2 and adult datasets separately. Raw counts subsetted from each sample were normalized with NormalizeData and FindVariableFeatures was used to define 2,000 variable genes in each. Reference 'anchors' across these datasets were obtained with FindIntegrationAnchors (with dims=1:50) and used to integrate the samples with IntegrateData. The ScaleData function was applied to scale and centre the integrated dataset, and to regress out as sources of variation the mitochondrial gene expression and the number of UMIs. Principal component analysis was run (with RunPCA) and the number of PCs was selected after inspection with ElbowPlot (nPCs = 20-40 depending on the dataset integrated). The clustering of cells was performed with FindNeighbors and FindClusters and the resolution was chosen after visually inspecting the resulting UMAP plot. Clusters were characterized with their common markers across LN stromal cells, defined using FindConservedMarkers (min.pct=0.25, min.diff.pct=-Inf, only.pos=TRUE). Genes differentially expressed between sample pairs were tested, cluster by cluster, with FindMarkers (default Wilcoxon Rank Sum test, logfc.threshold=-Inf). A heatmap with levels of expression of all DEGs (lfc > 1, fdr < 0.05) in all comparisons across LN districts for Cd34+ SC, Cxcl13+ SC and MuC E17.5 cells was made using pheatmap R package. Single gene expression UMAP plots were obtained with the FeaturePlot function. Heatmap plots of top marker genes and Dot-plots were obtained with DoHeatmap and DotPlot, respectively.

Label transfer procedure

Seurat3 supports the projection of reference data onto a query object. We have used this procedure, called 'label transfer' to infer the transcriptomic equivalence of E17.5 and P2 cell populations using the P60 adult dataset as a reference. The P60 reference anchors were used by the function *TransferData* to classify the query cells (E17.5 or P2) based on the reference data and returned a matrix with the predicted IDs and scores (Stuart et al., 2019). The evaluation of embryonic and neonatal cell populations assigned to the P60 adult clusters was presented as a heatmap of frequencies (in percentage) using the *pheatmap* function from the pheatmap R package while the *Sankey* rapresentations in Figure S8 were made using the *getSankey* function from the scmap R/Bioconductor package (Kiselev et al., 2018). The *Sankey* representation of the evolution of stromal cell populations of E17.5, P2 and P60 datasets in Figure 7 was made using the function *geom_alluvium* from the R package ggalluival.

Statistical analysis

Statistical analysis using a 2-tailed paired Student's *t* test was performed with GraphPad Prism 7.0 and values were expressed as mean ± SD. Differences were considered statistically significant at *P* less than 0.05 and details are provided in the figure legends.